Nuclear motion in molecular ions studied with synchrotron radiation and multicoincidence momentum imaging spectrometry

Laksman, Joakim

2012

Nuclear motion in molecular ions studied with synchrotron radiation and multicoincidence momentum imaging spectrometry

Joakim Laksman

Division of Synchrotron Radiation Research
Lund University

2012

Thesis for Degree of Doctor of Philosophy

LUND
UNIVERSITY

Doctoral Thesis

Division of Synchrotron Radiation Research
Department of Physics
Lund University

NUCLEAR MOTION IN MOLECULAR IONS STUDIED WITH SYNCHROTRON RADIATION AND MULTI-COINCIDENCE MOMENTUM IMAGING SPECTROMETRY

Printed in Lund, Sweden, February 2012, by MediaTryck

ISBN: 978-91-7473-272-6

Till Shan

Abstract

A momentum imaging spectrometer optimized for photoionization experiments with synchrotron radiation was built in 2008. The spectrometer is equipped with an electrostatic lens, that focuses the charged dissociation products on to a position-sensitive multi-hit delay line anode. The possibility of focusing is essential for most applications, where fragment momentum is to be extracted. The apparatus is equipped with a micro-channel-plate detector opposite to the delay line anode, enabling electron-ion coincidence experiments and thereby mass-resolved ion spectroscopy independent of the time structure of the synchrotron radiation. Calibration and characterization of the instrument is explained. Results for the photo-fragmentation of several molecules are presented, including measurements of kinetic and angular distributions as well as momentum correlations between coincident fragments. Various data analysis methods are described. High sensitivity of the instrument enables detection and analysis of weak processes such as isomerization. Full three-dimensional momentum information for each coincidence event is achieved which allows for in depth understanding of geometry, dynamics and energetics. In Ethyne, molecules with a *cis*-bending motion has been identified. In carbonyl sulfide and carbon dioxide, the Renner-Teller splitting has been analyzed. For the water molecule, transient isomerization has been found to be induced by strong bending vibrations in core-excited states. Also studies have been made on clusters, displaying the capability of the instrument to measure a large range of masses and kinetic energies.

Preface

The experimental work was performed at the beam-line I411 at the MAX-lab synchrotron radiation facility, Lund University, Sweden.

The dissertation consists of a summary of some general background together with the experimental and analysis methods used, followed by the papers containing the results:

I *Dynamics of proton migration and dissociation in core-excited ethyne probed by multiple ion momentum imaging*
J. Laksman, D. Céolin, M. Gisselbrecht, S. E. Canton and S. L. Sorensen
J. Chem. Phys. **131**, 244305 (2009)

II *Nuclear motion in Carbonyl Sulfide induced by resonant core excitation*
J. Laksman, D. Céolin, M. Gisselbrecht, and S. L. Sorensen
J. Chem. Phys. **132**, 144314 (2010)

III *Role of the Renner-Teller effect after core hole excitation in the dissociation dynamics of carbon dioxide dication*
J. Laksman, E. P. Månsson, C. Grunewald, A. Sankari, D. Céolin, M. Gisselbrecht, and S. L. Sorensen
To appear in J. Chem. Phys. (2012)

IV *Dissociation and isomerization after core-electron excitation in water*
J. Laksman, E. P. Månsson, A. Sankari D. Céolin, M. Gisselbrecht, and S. L. Sorensen
To be submitted to J. Phys. B (2012)

V *Development and characterization of a multiple coincidence ion momentum imaging spectrometer*
J. Laksman, D. Céolin, M. Gisselbrecht, and S. L. Sorensen
To be submitted to Rev. Sci. Instrum. (2012)

VI *Fission in liquid ammonia: from nano-droplet to a few molecules*
M. Gisselbrecht, **J. Laksman**, E. Månsson, C. Grunewald, A. Sankari, M. Tchaplyguine, O. Björneholm, and S. L. Sorensen
To be submitted to Phys. Rev. A (2012)

Comments on my own contribution to the papers

In all papers listed above I have contributed to the work. For all papers where I am the first author I have been responsible for the planning and making measurements as part of the scientific team, the analysis and a large part of writing the article. I have written the analysis routines used for

the multicoincidence studies. For the paper where I am not the first author, my contribution is reflected by the position in the author list.

Acknowledgments

This work could not have been accomplished without the assistance of several people.

I want to address thanks to my supervisors Stacey and Mathieu who have given me enormous support during my work and have conveyed the importance of experimental technique, electronics and careful analysis to me. I am indebted to Denis who has helped me with the experimental equipment at MAX-lab, as well as the design and characterization of the spectrometer. The contributions from the rest of the group are also greatly appreciated, so thanks to Erik, Anna and Noelle.

I must thank Franck for the informative explanation of the velocity imaging spectrometer. It has been a pleasure to work with Sophie, Klavs and Mikael at Gothenburg. I have appreciated the discussions with my room mates over the years: Suomi, Andrea, Evren, Sara, Jessica, Emilie, Rasmus, Tripta, Jan and Lassana. Also thanks to everyone else at the department: Ingolf, Jesper, Achim, Anders, Edvin, Patrik, Johan, Christina, Natalia, Olesia, Erik, Martin, Shilpi and Elin. Thanks to all the staff at MAX-lab: Maxim, Andras, Mikael, Bengt, Rami, Anders and others who have taken the time to help when needed.

Also I have enjoyed the time teaching at kurslab, so thanks to everybody there, especially the students without whom I wouldn't have had the chance to practice pedagogy.

Contents

Chapter 1

Introduction

The study of the motion of particles is ancient. The emergence of Newtonian mechanics about 400 years ago had far reaching applications for the development of technology and our understanding of the nature. The motion of objects, from mechanical components and projectiles to astronomical objects, such as satellites and planets is described by analytical equations in classical mechanics. Without accurate calculations of ballistic trajectories, artillery would never have been reliable and space travel would not be successful.

Classical mechanics provides accurate results as long as the domain of study is restricted to large objects. As the objects being dealt with become sufficiently small, it becomes necessary to introduce *quantum mechanics*, which treats particles as waves. The waves manifests themselves as probability for the particle to have a certain measurable. A range of phenomena than becomes possible that can not be explained with classical mechanics. An example is a rocket that can leave our planet only if it exceeds the escape velocity. In quantum mechanics however, this is not a constraint, so a particle may with a certain probability proceed through a barrier that is larger than the particles internal energy, which is referred to as quantum tunneling.

The objective here is to describe molecular dynamics in a quantum chemical picture. The energy gained by molecules after collisions with particles such as ions, electrons or photons can cause isomerization as well as a break up into neutral and charged fragments. The new compounds can lead to chemical reactions with its environment. An understanding of dissociation and isomerization processes is therefore useful in various scientific applications, such as the chemistry of surfaces and radiation damage in living tissue.

This thesis aims to give the reader knowledge regarding the concept of an ion momentum imaging spectrometer, and how it can be used to investigate a number of dynamic processes in molecules from a quantum chemical perspective. The physical picture of light interaction with small molecules is explained. Fundamental knowledge about core-electron excitation and the following Auger decay and fragmentation process gives us the possibility to define measurable quantities. From collected data we can then extract parameters that reveal a detailed description of the molecular geometry in the excited state. Illustrative examples are given from a number of small molecules. Since complete 3D kinematic information is measured, and these investigations are mostly concerned with the correlation of two or three fragments in coincidence from the same ionization event, the task is to extract easily interpretable quantities from the multidimensional data set. An emphasis is put on the anisotropy of molecular orientation with respect to the polarization vector of light and the kinetic energy released in the process. The most commonly used methods to present parameters and their correlation to each other, are explained. The spectrometer as well as the data treatment software have been developed in the group, therefore a significant part of this thesis is dedicated to the technological aspects of the work.

Chapter 2

Molecules and Clusters

2.1 Nuclear dynamics in molecules

A significant part of the results presented in this thesis concerns deformation and isomerization of molecules when interacting with electromagnetic radiation in the ultraviolet and X-ray domain. To understand these phenomena, a description of the molecular degrees of freedom is necessary.

2.1.1 Potential Energy Surfaces

A mathematical model that describes nuclear dynamics in molecules should be initiated by the simplest possible molecule which is a diatomic. Within a classical framework, the two atoms bonded together can be pictured as if they are connected via an elastic spring which can be stretched and compressed. They must therefore have an *equilibrium position*, r_e, where the potential energy reaches its minimum and no force is acting on them so their acceleration is zero. For the compressed and elongated regions however, the potential energy is large. As the elongation continues, the bond will break and the ball-spring model will no longer apply. Instead the potential energy will asymptotically approach the dissociation limit. A model for the physical properties of strong repulsion of the nuclei at small distances and the dissociation of the molecule which takes place at large internuclear distances is described by the *Morse potential*

$$V(r) = D_e \left(1 - e^{-\alpha(r-r_e)}\right)^2 \tag{2.1}$$

where r is the internuclear distance [1], D_e is the depth and α is a measure of the curvature of the potential well. This *Potential Energy Surface* (PES) is not symmetric around the internuclear equilibrium distance, see ground states (1) in Fig. 2.1. By solving the Schrödinger equation one obtains the eigenenergy values for vibrational level, n:

$$\begin{aligned} E_n &= \left(n + \frac{1}{2}\right)\hbar\omega_e - \left(n + \frac{1}{2}\right)^2 \hbar\omega_e x_e \\ \omega_e &= \frac{\alpha}{\pi}\sqrt{\frac{D_e}{2\mu}} \qquad | \qquad x_e = \frac{\hbar\omega_e}{4D_e}. \end{aligned} \tag{2.2}$$

where ω_e is the vibrational frequency and the quadratic term is a small anharmonic correction. The eigenenergy values are defined for $n \in \{0, 1, 2, ..., \infty\}$ and represent the quantized vibrational levels.

An ionization or excitation of a molecule puts it in an electronic state different from the ground state so the equilibrium distance will change. Initially, when the system is in thermal equilibrium, the vibrational levels are populated according to the exponential Boltzmann distribution, $N_i \sim e^{\frac{E_i}{k_B T}}$, where N_i is the probability, E_i is the energy, k_B is Boltzmann's constant and T is the temperature. Typically, the energy difference between two vibrational states is bigger then the denominator, $E_{i+1} - E_i \gg k_B T$, meaning that only the lowest vibrational state is populated.

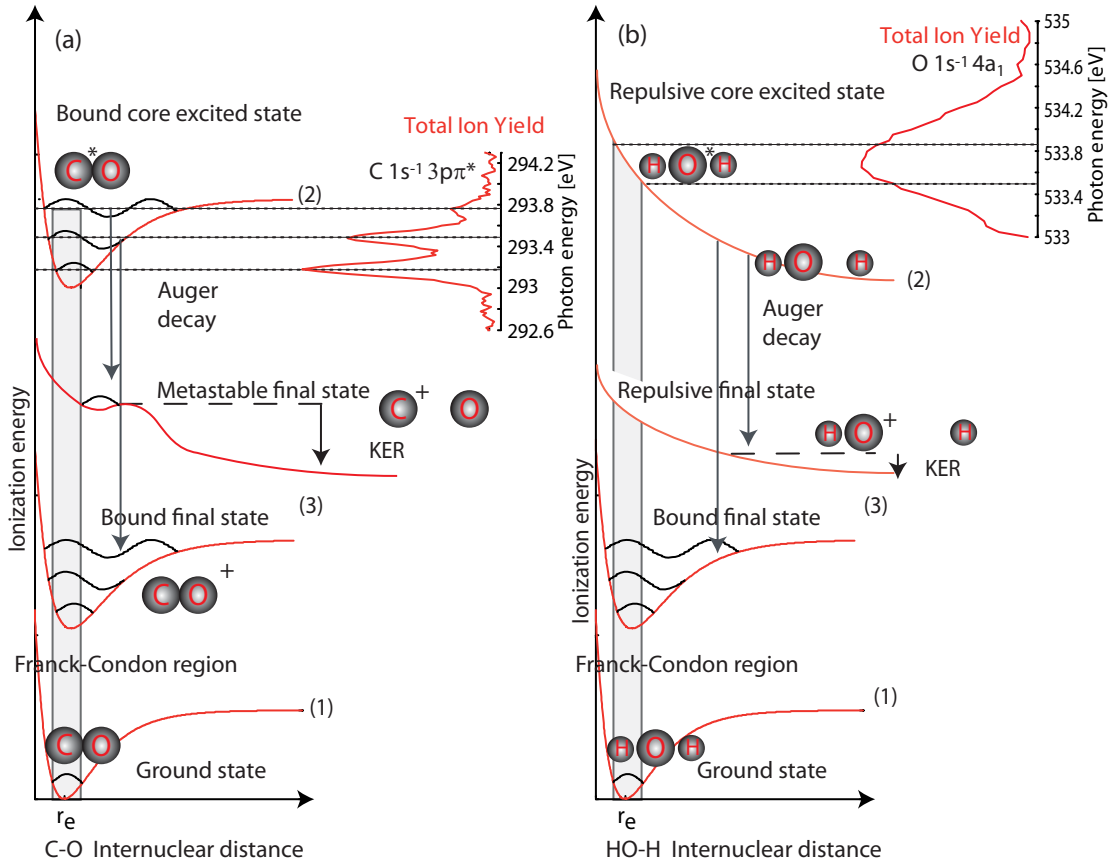

Figure 2.1: Energy level diagrams to schematically explain photo excitation and subsequent electronic decay in (a) the diatomic molecule carbon monoxide excited to the bound C $1s^{-1}3p\pi$ state. (b) the triatomic molecule water excited to the O $1s^{-1}4a_1$ state which is repulsive. The energy is not to scale. The inset shows a photon energy scan over the resonances and collection of the total ion yield spectrum, which is equivalent to absorption, reveals the vibrational structure. The intensity of the peaks reflect the overlap of the initial and intermediate wave-functions. r_e is the equilibrium bond distance in the ground state and the shaded region represents the Franck-Condon region. Dissociation processes are sketched in both cases. For both (a) and (b) decay to unstable states (3) leads to breakup where the fragments carry away the excess energy.

2.1.2 Direct ionization

The interaction between a photon and a molecule may lead to the emission of an electron with the kinetic energy E_K. The phenomenon of photoemission was detected by Hertz in 1887. A few years later, in 1905 Einstein was able to explain this phenomenon invoking the quantum nature of light where the photon quantum has the energy hf. The energy difference between the neutral ground

state and the ionized state E_B is given as

$$E_B = hf - E_K. \tag{2.3}$$

The kinetic energy of the electron, thus provides information regarding the state of the cation. If the incoming radiation has sufficient energy to remove a core electron, the cation will be in a highly excited state that subsequently will decay via electron emission and populate states in a multiply charged molecule.

2.1.3 Core-excited states

An indispensable concept in quantum chemistry is the *Born-Oppenheimer approximation*. It says that, during an electronic transition, the nuclei will, due to their compared with the electrons, larger inertia not have time to move, thus transitions are assumed to occur within the *Franck-Condon region* where the geometry is unchanged [1]. Vibronic transitions where the overlap of initial and final wavefunctions reaches its maximum are more likely to occur than others. Excitation from the ground state to an excited vibronic state can for example be accomplished with synchrotron radiation.

Fig. 2.1(a) presents a schematic of the core excitation and dissociation process of the diatomic carbon monoxide molecule, where only one stretch vibrational mode is required to describe the system. A technique to probe the PES of an excited state is to tune the radiation frequency over the particular resonance and collect all the produced cations. In the present work, a total ion yield was collected by scanning over the C 1s$\rightarrow$3pπ resonance for carbon monoxide where the first three vibrations are clearly resolved, see Fig. 2.1(a). The first peak, $\nu = 0$, is called the *adiabatic* peak and corresponds to transitions to the zeroth vibronic level in the C $1s^{-1}3p\pi$ state [2]. The second, $\nu = 1$, and third, $\nu = 2$, peaks accordingly represent transitions to the first and second excited vibronic levels. The adiabatic peak is the most intense, which means that its excited state wavefunction overlaps the most with that of the ground state. The more dominating the adiabatic peak is, the more similar are the initial and core-excited PES. The fact that also higher vibrations have a substantial intensity indicates, however, that the potential surfaces are somewhat shifted with respect to each other along the r_e coordinate. The peak energies in the spectra correspond to the eigenvalues in Eq. 2.2. By setting up the equation system $E_{n+1} - E_n$ for $n = \{0, 1\}$ it is thus possible to derive ω_e and x_e. The core-excited state than decays rapidly via Auger transitions, which populate electronic states in the cation.

Not all intermediate states are bound, if the contribution of antibonding orbitals outweighs that of bonding orbitals the PES will be dissociative, so no vibrational structure can exist. It is known from photoelectron spectroscopy experiments with water that the repulsive PES promotes elongation of one HO*–H bond and subsequent breakup to a neutral hydrogen atom and an excited OH fragment that auto-ionizes. This dissociation proceeds on a low femtosecond timescale and is said to be ultrafast [3]. In Fig. 2.1(b) an example is given of water excited to the O $1s^{-1}4a_1$ state. This is a cut through the three-dimensional PES along the HO*–H bond distance. Excitation occurs over the entire repulsive potential within the Franck-Condon region. The broad features in the total ion yield reflects this.

2.1.4 Auger decay

This work is about the study of multiple ion coincidences from molecules. For multiple coincidences to be possible, a multiple Auger decay is essential. Core-excited or ionized states are highly energetic and unstable intermediates that initiate decay via Auger processes. The decay follows an exponential density function within the same femtosecond regime as the fastest possible nuclear motion. Several deexcitation pathways are possible after inner-shell excitation or ionization. Regarding processes leading to dications after core excitation, two possibilities exists:

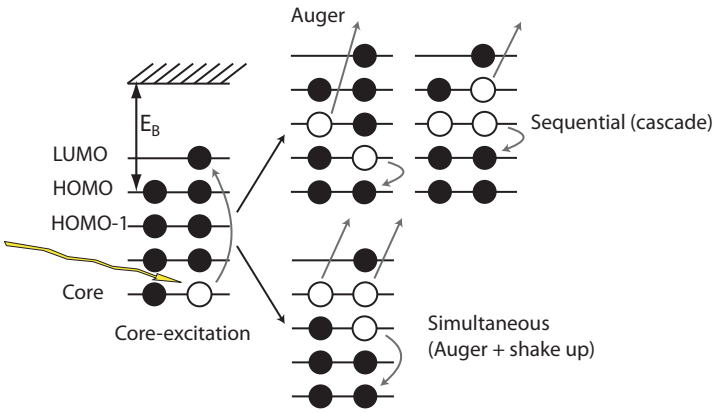

Figure 2.2: Schematic digram of the energy levels for core electron excitation. The subsequent electronic decay can be via Auger decay, Auger cascade decay or Auger accompanied by a shake-up process.

1: A simultaneous process observed for the first time by Krause [4] where the two electrons are ejected at the same time and share continuously the available excess energy.
2: A sequential process, where the charged ion state populated in the first Auger decay is autoionizing and releases a second electron [5]. After the first decay, further nuclear motion can proceed within the cationic state, thus sending the wave-packet to remote areas of the PES that otherwise would not be explored. One possibility is a repulsive state in the excited cation that can not emit a secondary electron due to the strong attractive Coulomb force until after breakup into one charged and one excited fragment where the latter subsequently autoionizes, thus finally producing two cationic fragments [6, 7].

Fig. 2.2 presents schematic diagrams of the two processes. Triply, quadruply and more highly ionized states can be reached with combinations of these pathways, assuming that the energy of the initially excited ion is sufficient for the triple (or higher) ionization threshold. If the process instead is initiated by core ionization, the Auger decay is analogous, but the end product has one less electron.

An instrument that detects and energy analyzes multiple electrons in coincidence is the *magnetic bottle* spectrometer. It allows energy correlation studies which can reveal the different decay mechanisms [8]. In this study however, no energy analysis is made on electrons, so there is no possibility to distinguish between these processes.

2.1.5 Final states

After an Auger decay, the molecule is multiply charged. If the electronic states of the system is bound, stable charged states of the parent molecule are produced. Typical energies of Auger electrons are a few 100 eV, so considering conservation of momentum, the kinetic energy of these molecular ions is a few meV, similar to their thermal energy in room temperature, thus no information regarding the electrons can be deduced, regardless of the sensitivity of the instrument.

If, on the contrary, the excited molecule decays to a repulsive final state, breakup follows with the charges located on one or more fragments. The difference in potential energy between the final dissociative state and that of the fragments, is converted into kinetic energy carried off by the fragments, see schematic in Fig. 2.3. The *Kinetic Energy Released* (KER) is related to the fragment's velocity, v, as KER$= \sum_i \frac{m_i v_i^2}{2}$ where m_i is the i^{th} particle's mass. A measurement of fragment velocity can thus reveal information about the final dissociative states that are populated. With the momentum imaging spectrometer that was used for these experiments, the velocity of

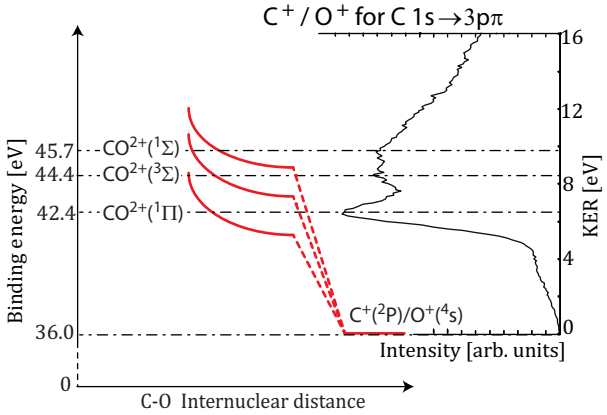

Figure 2.3: KER distribution from CO after core-excitation to the C $1s^{-1}3p\pi$ state and breakup to C^+/O^+. Three peaks are distinguished. They are assigned by considering the difference in potential energy between final states and the fragments ground states.

each fragment can be measured and thus one can find some information regarding the transitions. Fig. 2.3 presents a KER distribution from CO after core-excitation to the C $1s^{-1}3p\pi$ state and breakup to C^+/O^+. Three peaks can be distinguished. Assuming that the cationic fragments are in their ground states $C^+(^2P)/O^+(^4S)$ at 36 eV above the neutral ground state it is possible to assign the final states [9, 10]. This will be explained more in detail in Sec. 4.2.1.

Another possibility is *metastable* states, where the potential well is very shallow [11]. The wavepacket will remain there for a while but inevitably tunnel out eventually, see schematic in Fig. 2.1(a). The lifetimes of metastable states which are typically a few μs can be measured. A vibration takes place on tens of fs so the number of vibrational cycles of the state can be estimated, which is typically several millions [2, 12].

2.1.6 Vibrational modes

In order to describe the vibrational motion of polyatomic molecular systems, a more generalized model is required. Since each atom has three degrees of freedom, the PES of an N-atomic molecule is a function of $3N$ variables. Translations of the entire compound in any direction have no impact on relative interatomic positions, so by selecting a suitable coordinate system, the number of variables can be reduced with three. Additionally, there are three spatial rotational symmetry-axes that each can reduce the number of variables further. In the special case of linear molecules, only two rotational axes are relevant, thus the PES can be described with $3N-5$ dimensional coordinate system where the axes are vibrational modes. Observe that for the diatomic case there is $3\cdot2-5=1$ vibrational mode, exactly as was shown for carbon-monoxide previously. The linear tetra-atomic ethyne molecule, C_2H_2, that belongs to the $D_{\infty,h}$ point group has a PES with $3\cdot4-5=7$ vibrational modes as shown in Fig. 2.4(a). The conventional assignments found in the literature [1, 13, 14] are as follows: ν_1 (symmetric CH stretch), ν_2 (symmetric CC stretch), ν_3 (antisymmetric CH stretch), ν_4 (two degenerate *trans* bend), ν_5 (two degenerate *cis* bend). For nonlinear molecules where all three rotation axis must be taken into consideration the PES reduces to $3N-6$ dimensions. An example is water in the neutral ground state which belongs to the C_{2v} point group (Fig. 2.4(b)). Three modes are sufficient: ν_1 (symmetric stretch), ν_2 (bend) and ν_3 (asymmetric stretch). Each of these modes can be populated with a number of vibrational levels, thus for polyatomic molecules, a vibronic state must be described as a vector property. In H_2O, promo-

tion of the oxygen core electron to the bent $2b_2$ orbital is therefore denoted as O 1s$\rightarrow 2b_2^*(\nu_1, \nu_2, \nu_3)$.

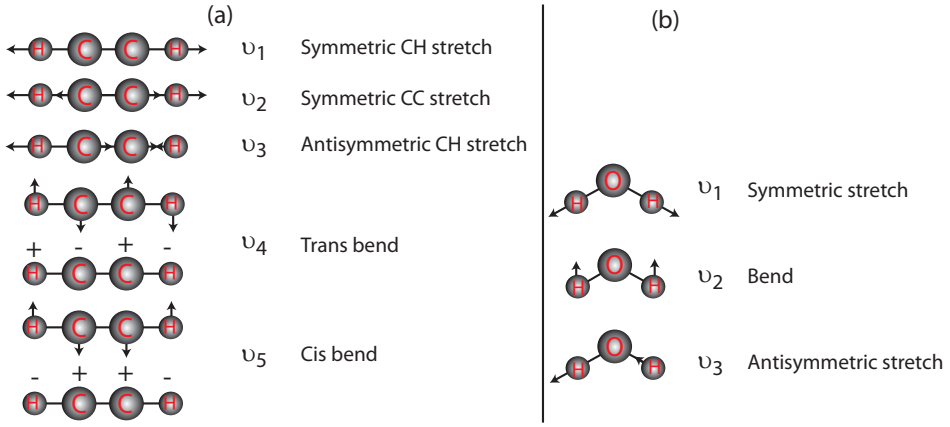

Figure 2.4: (a) For a linear quad-atomic molecule belonging to the $D_{\infty h}$ point group, such as C_2H_2 there are $(3 \cdot 4 - 5) = 7$ vibrational modes, whereof two pairs are degenerate, so we need a total of five labels. (b) For a bent tri-atomic molecule belonging to the C_{2v} point group, such as H_2O there are $(3 \cdot 3 - 6) = 3$ vibrational modes, so we need a total of three labels.

2.1.7 Transition probability

The permanent dipole moment $\vec{\mu}$ is a vector quantity. Interaction between molecules $\vec{\mu}$ is a significant contribution to the Van der Waals force and is therefore of major interest in the study of intermolecular interactions. Only by molecules belonging to the point groups C_n, C_s and C_{nv} have a permanent dipole moment. The presence or absence of $\vec{\mu}$ therefore provides some information about the molecular symmetry. For example, carbonyl sulfide (OCS) that belongs to $C_{\infty v}$ is expected to have $\vec{\mu} \neq 0$ since oxygen and sulfide have different electro-negativities, so it is called a polar molecule. Ethyne (C_2H_2) in the ground state from the $D_{\infty h}$ point group must have zero dipole moment [15].

In the field of molecular dynamics, angular information is essential to the understanding of the light-molecule interaction. Zare and Herschbach [16, 17, 18] showed that for polarized light the interaction probability for a transition between an initial and final electronic state with wavefuctions ψ_i and ψ_f, should have a connection to the vector correlation between the electric field vector $\vec{\epsilon}$, and the molecules transition moment $\vec{R^{if}}$. The probability P_{if}, is usually expressed with Fermi's Golden Rule that describes the interaction as the the square of the scalar product,

$$P_{if} = (\vec{R}^{if} \cdot \vec{\epsilon})^2 \tag{2.4}$$

Within the dipole approximation, that is valid for linear molecules, the transition moment is the vector

$$\vec{R}^{if} = \int \psi_i^* \vec{\mu} \psi_f d\tau, \tag{2.5}$$

where the integration is over all space, (for more complicated molecular configurations terms from the quadropole or even octopole approximation must be included). $\vec{\mu}$ is the permanent electric dipole moment, given as the sum of all charges q in the system multiplied by their respective distance from the center $\vec{r}$, so $\vec{\mu} = \sum_i q_i \vec{r_i}$ [1]. Eq. 2.4 and Eq. 2.5 means that the transition probability is only dependent on the angle between these two vectors. The direction of $\vec{R}^{if}$ is

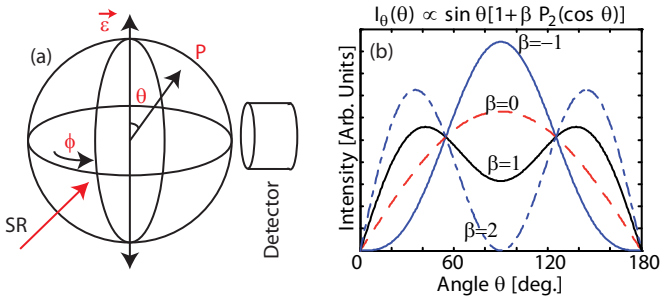

Figure 2.5: (a) The zenith angle θ is defined with respect to the polarization vector $\vec{\epsilon}$. ϕ is the azimuthal angle, p is length of the vector that is related to the fragments kinetic energy. The synchrotron radiation (SR) is perpendicular to $\vec{\epsilon}$ and the detector axis. (b) Normalized intensity distributions as a function of θ for some selected β parameters.

well defined and fixed for a certain transition, meaning that P_{if} strongly depends on whether the molecular symmetry axis is parallel ($\Delta\Lambda = 0$; for example C1s$\rightarrow \sigma^*$ excitation) or perpendicular ($\Delta\Lambda = \pm 1$; for example C1s$\rightarrow \pi^*$ excitation) to the polarization.

Provided that the *axial recoil approximation* is valid, meaning that the fragmentation takes place rapidly enough for the alignment not to be lost before the breakup, the anisotropy will be reflected in the fragment recoil momentum vector $\vec{p}$. Fig. 2.5(a) shows the geometry of the system coordinates. The zenith angle θ is defined with respect to $\vec{\epsilon}$. ϕ is the azimuthal angle and p is the momentum vector length. The synchrotron radiation propagation vector (SR) is perpendicular to $\vec{\epsilon}$ and the detector axis.

Zare derived the spherical intensity distribution

$$I_{\theta,\phi}(\theta,\phi) = \frac{1+\beta P_2(cos\theta)}{4\pi} \tag{2.6}$$

where $P_2(x)$ is the second-order Legendre polynomial $P_2(x) = (3x^2-1)/2$. β is the anisotropy parameter that characterizes the angular distribution, depending on the radiative transition symmetry in the molecule. This parameter can vary from -1 for a purely perpendicular transition to $+2$ for a purely parallel transition[19, 20, 21]. $I_{\theta,\phi}(\theta,\phi)$ is normalized so that

$$\int_{\theta=0}^{\pi}\int_{\phi=0}^{2\pi} I_{\theta,\phi}(\theta,\phi)d\phi d\theta = 1. \tag{2.7}$$

Considering the cylindrical symmetry around $\vec{\epsilon}$, an integration can be performed over ϕ without any loss of information. The normalized distribution over the polar angle then becomes:

$$I_\theta(\theta) = \frac{\sin\theta[1+\beta P_2(cos\theta)]}{2}. \tag{2.8}$$

In molecules where the ground state is Σ, $\beta = 2$ corresponds to $\Sigma \rightarrow \Sigma$ transitions while $\beta = -1$ corresponds to $\Sigma \rightarrow \Pi$ transitions [22]. Fig. 2.5 (b) shows normalized intensity distributions as a function of θ for some selected β parameters. $\theta = 54.7°$ is called the magic angle since all intensities intersect. It can be used when no dependence on the angular distribution is desired [23].

Section 4.2.4 treats how the momentum imaging spectrometer can be used to measure the anisotropy parameter. Also some examples are given that illustrate how it can provide us with information regarding the alignment of the core excited state.

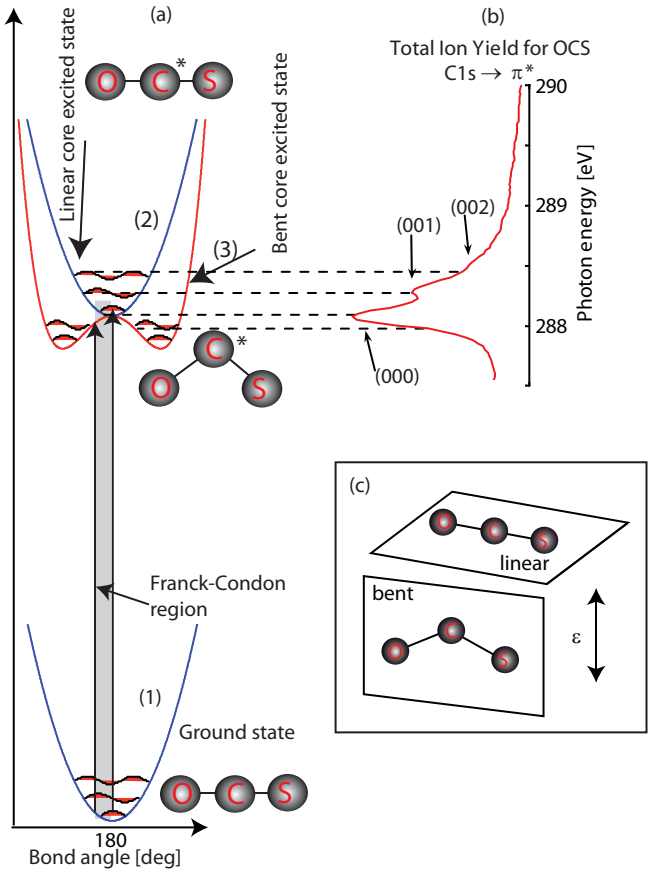

Figure 2.6: (a) Schematic representation of the potential energy curve for a triatomic molecule as a function of the bending coordinate. The ground state (1) is linear, but the Renner-Teller effect splits the excited state into one with linear (2) and one with bent (3) equilibrium geometries. (b) Total Ion Yield from OCS at the C1s→ π^* resonance, where three vibrations can be distinguished. The Franck-Condon factor is larger for a linear-to-linear, then for a linear-to-bent transition, but at the low energy side of the (000) vibration, the bent excited state might be more likely. (c) The bending plane of molecular geometries for linear and bent symmetries.

2.1.8 Renner-Teller splitting

For linear polyatomic molecules with degenerate electronic states, the Renner-Teller effect must also be taken into consideration. The Renner-Teller theorem states that a linear molecule can not remain stable in a degenerate state, thus a geometrical distortion will lift the degeneracy. This distortion induces new vibrational modes in the molecule, so it can happen that the equilibrium geometries of the core-excited states are different from that of the neutral ground state. As a consequence, asymmetric nuclear motion can be induced in the excited states, which plays an important role in the decay processes and can open up new dissociation pathways that are not reachable in the molecules initial geometry [24]. Fig. 2.6(a) presents a schematic representation of the potential energy curve for the triatomic molecule OCS as a function of the bending coordinate. The ground state (1) is linear, but the Renner-Teller effect splits the C $1s^{-1}\pi^*$ core excited state into one with linear (2) and one with bent (3) equilibrium. In Fig. 2.6(b) total ion yield for the C1s→ π^* resonance is presented, where three vibrations can be distinguished. The Franck-Condon factor is larger for a linear-to-linear, then for a linear-to-bent transition, but at the low energy

side of the (000) vibration, the bent excited state has a significant probability to be populated [25]. This resonance is a $\Sigma \rightarrow \Pi$ transition where the linear molecule is in the plane perpendicular to $\vec{\epsilon}$. This implies that the bending vibrations of the linear state also lie in this plane. Dipole considerations however constrains the bent state to vibrate in a plane parallel to $\vec{\epsilon}$. See Fig. 2.6(c).

Moreover, the core-excited state can be described by the *equivalent core* or $Z+1$ approximation, where the effect of the core hole on the valence electrons is modeled as an increase of the nuclear charge, Z, by one unit. The atom containing the core-hole is thus replaced by the one with charge $Z+1$. Core excited OC*S will thus have chemical and physical properties similar to ground state of ONS which is known to be bent [26].

2.1.9 Molecular orbitals

Calculations of energies of electronic states for atoms is accomplished by solving the Schrödinger equation for the system. For molecules, the interaction between several atoms is included and spherical symmetry is lost. Atomic orbitals for many-electron atoms are used to construct molecular orbitals. If the interaction of two individual atoms that approach each other lowers the total energy of the system, a covalent bond is formed. Consequently, the involved atom's electronic structure will be rearranged and combined into molecular orbitals. The most often used approach to describe the electronic structure of molecules is as *linear combinations of atomic orbitals*[27, 1].

As an illustrative example of how to construct the electron structure we start with the linear triatomic OCS molecule. The conventionally defined coordinate system is with the z-axis is parallel to the symmetry-axis of the molecule. When assigning molecular orbitals we use lower-case Greek letters. σ tells us the the orbital is symmetric with respect to a plane in the z-axis. π means anti-symmetric with respect to that plane. The three constituents of OCS have sufficient nuclear charge for the core electrons to be highly localized. The first orbital is $1\sigma^2_{S(1s)}$ where the subscript indicates that it is localized to the sulfur atom, and the superscript indicates that according to the Pauli-principle, two electrons can populate this electronic state (spin up and spin down). Due to the other atoms in the molecule, the electron's wavefunctions are different from that of the atom, therefore the energy of the state has a chemical shift. The second and third orbitals are accordingly $2\sigma^2_{O(1s)}$ $3\sigma^2_{C(1s)}$. The fourth highest binding energy has been found to be the S2s localized orbital, so we have $4\sigma^2_{S(2s)}$. The next orbital is the S2p, and is more complicated. In the free atom, the three directions (x,y,z) are indistinguishable, but in the molecule, this is not the case. S2p$_z$ has σ character, so the fifth orbital becomes $5\sigma^2_{S(2p_z)}$. S2p$_{x,y}$ are anti-symmetric in a plane parallel to the z-axis, so they give us the first π orbital $1\pi^4_{S(2p_{x,y})}$. Now the localized core orbitals are filled and we start with the valence orbitals. Symmetry and other considerations impose some constraints regarding the construction of molecular valence orbitals. O2s and C2s orbitals both have σ symmetry, they have similar binding energies and they overlap, so they combine into a bond that in carbon monoxide would be designated 3σ. The valence orbital $6\sigma^2_{CO(3\sigma)}$ is thus created. The remaining orbitals are delocalized valence orbitals $7\sigma^2 8\sigma^2 9\sigma^2 2\pi^4 3\pi^4$. To conclude, the electronic orbital ground state occupation can be written as [28]

$$1\sigma^2_{S(1s)}2\sigma^2_{O(1s)}3\sigma^2_{C(1s)}4\sigma^2_{S(2s)}5\sigma^2_{S(2p_z)}1\pi^4_{S(2p_{x,y})}6\sigma^2_{CO(3\sigma)}7\sigma^2 8\sigma^2 9\sigma^2 2\pi^4 3\pi^4 \quad {}^1\Sigma^+. \tag{2.9}$$

For molecules from the $D_{\infty h}$ point group such as ethyne, orbitals are assigned with an additional label: *gerade* (g) or *ungerade* (u) indicating inversion symmetry of the wavefunction through the molecules center. Combination of two $1s$ atomic orbitals that overlap gives $1\sigma_g$ and $1\sigma_u$, each of which can be occupied by one spin up and one spin down, so the ground state configuration for ethyne is [29]

$$1\sigma_g^2 1\sigma_u^2 2\sigma_g^2 2\sigma_u^2 3\sigma_g^2 1\pi_u^4 \quad {}^1\Sigma_g^+. \tag{2.10}$$

For classification of electronic states in molecules, the atomic Russel-Saunders notation's Greek equivalents are utilized. The orbital motion of each electron induces magnetic moments that

interact with each other to give a quantum number that is defined for all non-negative integer values $\Lambda \in 0, 1, 2, ...$ with the designated symbols Σ, Π and Δ. For ethyne the filled σ configurations carry no orbital angular momentum and the π^4 orbitals must contribute 0 to Λ since it has two electrons orbiting in each direction, so the term value is Σ. Because terms designated Σ can be composed of π orbitals, a label is required that distinguishes between symmetry and anti-symmetry under a σ_v operation. σ orbitals have the character $+1$ under this reflection, while if four electrons populate the π orbitals, two will have -1 and two will have $+1$ as character, and the overall character will be $+1$, which then becomes the right superscript. The spin multiplicity of the state has the value 1, meaning it is a singlet because all electrons are paired, so only one spin combination is possible, which gives us the left superscript. The overall parity of the state is g because there are even numbers of both gerade and ungerade for each individual electron. Accordingly, the ground state configuration of ethyne is ${}^1\Sigma_g^+$.

2.2 Clusters

When several atoms or molecules come sufficiently close to each other they form bonds and become clusters whose size can range from a few to millions of monomers. The purpose of cluster studies is to analyze the gradual development of the molecules size-dependent collective properties that characterize the bulk which can be a liquid or a solid. Primarily electrostatic dipole-dipole interaction is responsible for bond-formation. In molecules such as NH_3 where a number of hydrogens are covalently bonded to an electronegative atom, hydrogen bonding is the dominating contribution, but also *Van der Waals* forces play a significant contribution [30]. Ammonia can be generated by evaporation, condensation and supersonic expansion into a jet-beam. Singly charged ammonia clusters have an NH_4^+ core surrounded by layers of 4 NH_3 molecules in each sub-shell [30, 31]. The dissociation process for multiply charged clusters is different compared to that for molecules. After the Auger process, two localized charges will repel each other and subsequently migrate to opposite ends of the cluster followed by Coulomb explosion. The larger the cluster is, the further apart are the charges at the time of breakup, thus leading to less kinetic energy [32].

Another example are the stable fullerenes which has a polygon structure, especially famous is C_{60}. For C_{60}^{q+} a multi-step sequential evaporation process of neutral carbon dimers have been found to be dominating [33, 34, 35].

Chapter 3

Experimental

3.1 Momentum imaging spectrometer

The modern high-resolution momentum imaging spectrometer that is utilized by research groups all over the world and is described in this section has evolved from many years of successive developments and improvements. Already in the 1950s the concept of the ion *Time of Flight* (TOF) spectrometer was established. The basic idea is that charged particles are accelerated through regions with static electric fields that cause dispersion in time due to their different inertia, thus a spectrum is produced in time. When presented in a histogram, the peak width is related to the distribution in initial kinetic energies, while the peak shape is related to the anisotropy [36]. A breakthrough came when Wiley and McLaren [37] constructed a prototype and derived a mathematical foundation for an analytical treatment of ion trajectories, with which they could minimize the spatial dependence of molecules initial position. *Time to Digital Converters* (TDC) with higher sampling rate frequency and the possibility to measure several ions from each ionization event allowed the Eland group [38, 39, 40, 41, 42, 43, 44, 45, 46, 47, 48] to make further advancements in the field. Contributions were also made by Ueda [49] who by applying a pulsed field over the extraction region increased the dispersion and thereby also the kinetic energy resolution.

In parallel with the TOF developments, a different type of dispersion element emerged: The imaging technique where a position sensitive detector registers the ion's two other momentum coordinates. Since its introduction in the field of molecular spectroscopy imaging has had a significant impact on the research of molecular dynamics. By using the Abel transform, Chandler *et al.* [50] and Eppink *et al.* [51] were able to extract kinetic and anisotropic information from dissociation processes in molecules using lasers for excitation. Due to the slow sampling rate ($\sim 1\mu$s) of the fluorescent screens used in these first setups, no temporal information could be extracted.

To eliminate this constraint, Eland *et al.* [52] introduced a radial position sensitive detector for ion TOF coincidence measurements, that made it possible to extract correct KER distributions. Further development of delay line anodes (DLD) was made in two dimensions [53]. With access to both temporal and spatial data, particles complete kinematic information can be extracted, so these two techniques were combined and the momentum imaging spectrometer was born [54]. More recently, further improvements in the field regarding spatial resolution were made by Céolin *et al.* [55, 56].

Our linear momentum spectrometer consists of a two-field acceleration system and a commercially available detector-system produced by RoentDek [53]. The spectrometer design was done with the computer program, Inventor, a parametric mechanical design CAD application developed by Autodesk. It allows users to create detailed technical drawings and 3D models for prototype

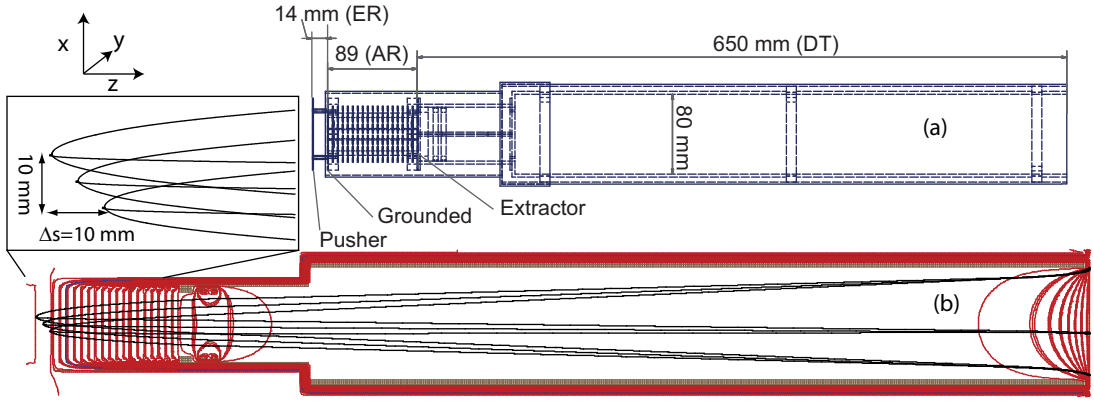

Figure 3.1: (a) CAD drawing of flight-tube for Wiley-McLaren linear momentum multiple coincidence spectrometer. Molecules are ionized in the Extraction Region (ER) where a field is applied so that the Pusher attracts electrons but repels cations. Ions continue through the Acceleration Region (AR) and Drift Tube (DT). From flight time and position we can derive momentum. (b) Simulation made in SIMION of cation trajectories in the flight-tube with typical applied voltages. Due to the focusing conditions, irrespective of the initial position (Δs), all ions with a certain momentum vector hit the detector at the same position and instant in time.

development and manufacturing. Additionally, it features the possibility to export assembly files to other applications, which allows for interaction with other models as well as customized simulations, for example charged particle trajectories with voltages applied on the electrodes [57].

3.1.1 Flight tube

Studies of formation and fragmentation dynamics of molecular cations created in gas phase single photon ionization generally require coincidence experiments for their investigation. For these measurements, a *Wiley McLaren Time Of Flight* (TOF) mass-spectrometer, equipped with a *delay-line anode* for position-sensitivity, was constructed [58, 37]. The flight-tube consists of the three sections: *Extraction region* (ER), *Acceleration Region* (AR) and *field-free Drift Tube* (DT). Their dimensions along the drift-axis are 14, 89 and 650 mm respectively, see Fig 3.1(a). To protect ion trajectories from the influence of external electric fields that can produce noise, an aluminum cylinder encloses the flight tube, working essentially as a Faraday cage. The spectrometer is accommodated in a stainless steel vacuum chamber, that is mounted on a steel frame with rails which permits 2D adjustments in the horizontal plane.

The ionizing radiation intersects an effusive jet of target gas in the ER so that electrons and ions are extracted from the center in opposite directions by a strong DC electric field. The electrons impinge on a *Micro Channel Plate* (MCP) mounted next to the ER. It enhances the signal with by factor of $\sim 10^7$ that is then detected on an anode, thereby starting a timer. The ions, after passage through the ER, gain additional velocity in the AR and thereby enter the DT. After leaving the DT, the cationic molecular fragments are separated in time according to their mass/charge ratio, $\frac{m}{q}$. They are then also detected by a MCP.

One must consider that when applying too weak electric fields, ions will have time to escape the spectrometer, limiting the 4π steradian collection. Too strong fields on the other hand will decrease both the time and radial distribution, and therefore also the momentum resolution. A compromise between these parameters depending on ejected fragments KER must be found.

In order to avoid field penetration, that affects ion trajectories, it is desirable to have as homogeneous electric fields as possible. At the borders between the three regions where the field gradient is large, this is accomplished with grids. Fig. 3.1(b) shows field lines as a contour plot generated

with the commercially available software SIMION [59]. Due to the grids 80% transmission efficiency however, we chose not to put one at the end of the DT, with the consequence that ions are deflected by the potential gradient. The ER is short enough for field penetration to be insignificant, but for AR, this must be compensated for. Between the grounded electrode and the DT, in Fig. 3.1(a), 17 electrode-rings are evenly spaced. They are interconnected with 18 serial resistors with 1 MΩ each. A typical applied voltage V on the DT is -4 kV, thereby exposing the voltage supply to the power $P = \frac{V^2}{R} = \frac{(-4kV)^2}{18M\Omega} \simeq 0.9$ W. The resistance R is selected to avoid exceeding the maximum power of the power supply that is rated at 8 W [60].

3.1.2 Focusing

The ionization volume where the radiation intersects the effusive beam is not a point, but has a distribution of a few mm, with the consequence that two identical ions with identical momentum vectors, created at slightly different points, will not necessarily reach the detector at the same instant or at the same position. Each ion is measured as a flight time and a position on the detector. The coordinates we register depend on the initial position of ion creation in the ionization volume as well as the linear momentum gained from the dissociation. We are interested in measuring particle's momentum, thus we want to minimize space dependence on peak shapes. For that, focusing is required. A separation between TOF and position focusing can be made.

Time focus

A Cartesian coordinate system, (x, y, z), is suitable to describe a particles position in the source region, where z is parallel to the spectrometer axis. If all ions were formed in the (x, y) plane parallel to the source electrodes, the flight time would be the same for all ions with the same velocity and $\frac{m}{q}$, so the resolution would only be limited by the detecting equipment. In practice, the spectrometer's resolving power in time depends on its ability to reduce the spread caused by the ever-present initial space distribution Δs, that can be considered as a deviation from the ionization volume center, see Fig. 3.1(b). The time resolution objective is to reduce the time spread, ΔT, caused by this spatial distribution. This can to some extent be accomplished by making Δs small, but applying a certain voltage ratio over the electrodes that introduces a time lag between the creation of the ions and their acceleration. Ions placed behind the source point center will travel a longer distance through ER, but since they also will be exposed to the electric field for a longer time, they will travel faster. The problem is therefore to find parameters where these two effects cancel each other out so that the final TOF is unaffected by the initial position. The time T it takes an ion with initially zero kinetic energy to travel through the flight-tubes three regions was derived by Wiley and McLaren [37] as

$$\begin{aligned} T_{ER} &= \sqrt{\frac{2ms}{qE_{ER}}} \\ T_{AR} &= \frac{\sqrt{2mqsE_{ER} + 2mqdE_{AR}} - \sqrt{2mqsE_{ER}}}{qE_{AR}} \\ T_{DT} &= \frac{\sqrt{2m}D}{\sqrt{qsE_{ER} + qdE_{AR}}} \\ T &= T_{ER} + T_{AR} + T_{DT}, \end{aligned} \tag{3.1}$$

where s is the length of the ions path in ER, d is the length of AR and D is the length of DT. To minimize the dependence on the initial location, we must fulfill the boundary condition $\frac{\partial T}{\partial s}\big|_{s=s_0} = 0$, where s_0 is the distance from the ionization volume center to the AR entrance. If we define k_0 as

$$k_0 = \frac{s_0 E_{ER} + dE_{AR}}{s_0 E_{ER}}, \tag{3.2}$$

we obtain the following relationship between the length of the regions and the electric fields:

$$D = 2s_0(k_0)^{\frac{3}{2}} \left(1 - \frac{1}{k_0 + \sqrt{k_0}} \frac{d}{s_0}\right). \tag{3.3}$$

This focus condition is the same for all ions irrespective of their energy. The lengths of the regions are fixed so the ratio of the electric fields $\frac{E_{AR}}{E_{ER}}$ is uniquely determined by Eq. 3.3. The voltages, V, over the electrodes are related to their spatial separation and the desired homogeneous fields. For our specific conditions, we numerically find the ratio

$$\frac{V_{AR}}{V_{ER}} = -9.97. \tag{3.4}$$

This value is in good agreement with our simulations, and was also confirmed empirically.

Furthermore, observe from Eq. 3.1 that T follows the relation

$$T = a + b \cdot \sqrt{\frac{m}{q}}, \tag{3.5}$$

where a and b are constants depending on the electrodes in the spectrometer and the electric fields. m and q are the ions mass and charge respectively.

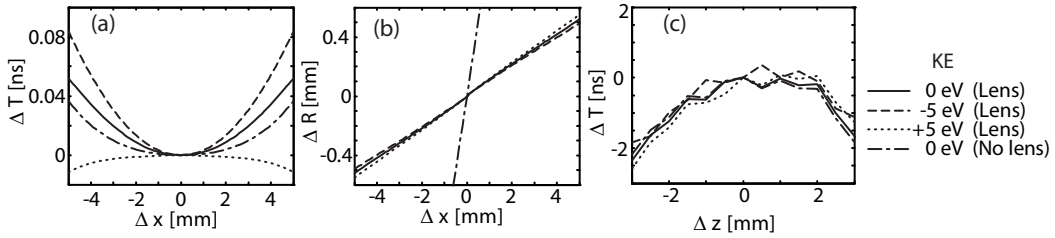

Figure 3.2: To characterize the instruments focusing capability depending on the source volume, simulations were made. (a) Deviation in TOF, ΔT, as a function of the molecules position in the direction perpendicular to the spectrometer axis, Δx. (b) Deviation in hit position, ΔR, as a function of Δx. (c) ΔT as a function of the molecules position in the direction parallel to the spectrometer axis, Δz.

Position focus

An electrostatic lens that focuses charged particles for momentum imaging was first developed by Chandler et al. [50] for studies of the velocity distributions of ions. Eppink and Parker [51] improved the lenses by a system composed of three electrodes with an open hole to increase transmission efficiency, trajectory precision and image resolution. This modification of the momentum imaging technique has made it one of the indispensable tools in the field of molecular reaction dynamics. Our system is based on this technology. Due to the complexity of the electric field gradient produced by the lens and also the field penetration in the end-section of the DT, no analytical expression could be derived to find desired voltage combinations. Instead this was accomplished both empirically and with numerical simulations. In general, no linear relation between the lens voltage V_L and the other voltages can be expected, but when time focus is valid, for V_{AR} in the typical interval -2000 V to -5000 V the ratio

$$\frac{V_{AR}}{V_L} = 1.23 \tag{3.6}$$

turned out to hold with sufficient precision. In Fig. 3.1(b), we present a simulation where a cubic source volume of 10 mm was used. Cations with a mass of 10 a.m.u. are ejected with 12 eV

in various directions (70°,90°,170°) with respect to the center axis. It is seen that the potential difference between the lens electrodes and the surrounding DT creates an electrostatic bubble that guides ions with identical linear momentums to a $\lesssim$ 1mm sized spot on the position-sensitive detector (PSD), even when the ions are produced at very different positions in the ionization volume.

Overall focus
Our objective is to combine these two focusing conditions. However, optimization of the TOF focusing can distort the position focusing and vice versa, thus to diagonalize the problem completely might not be achievable. Instead we look for a good compromise. In Fig. 3.2 we analyze the dependence of ΔT and ΔR as a function of the the source region and different kinetic energies: 0 eV (solid line), 5 eV along spectrometer direction (dotted), 5 eV opposite the spectrometer direction (dashed). Also we compare with the lens turned off (dash dotted). Fig. 3.2(a) shows that a variation of $\Delta x = \pm 5$ mm and KE= ± 5 eV leads to a ΔT that never exceeds 0.1 ns and that the impact of the lens is not significant. In Fig. 3.2(b) it can be seen that under the same conditions $\Delta R = \pm 0.5$ mm, and is mainly unaffected by the kinetic energy, but a comparison with the lens unactivated illustrates the focusing effect. Fig. 3.2(c) shows ΔT as a function of the source region deviation parallel to the spectrometer axis, Δz. Around $\Delta z = 0$ there is a plateau, where time focusing is achieved. Δz is only constrained by the width of the radiation beam which is less than 1 mm. For all KE, focusing is maintained. More significant is that activation of the lens has no impact on the Wiley McLaren condition, thus showing that indeed, our approach of separating focusing into time and position components is valid.

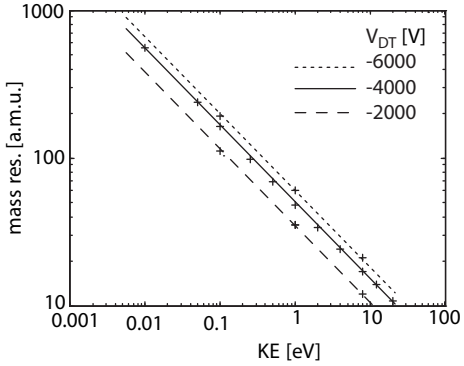

Figure 3.3: Simulated maximum mass resolution as a function of kinetic energy for different voltage settings on a logarithmic/logarithmic scale that covers a large range of both energies and masses. Lines have been fitted to the data points. Indeed, it is interesting that the relation agrees well with the linear function.

3.1.3 Mass resolution

The capacity of a TOF spectrometer to separate ions with adjacent $\frac{m}{q}$ ratio constitutes its mass-resolution [61]. The larger fragments one want to resolve, the less kinetic energy they must have. The objective during development of the spectrometer was an ability to study a large range of masses and kinetic energies. Its purpose is to analyze high energetic small molecular fragments as well as low energetic clusters. In order to resolve large masses, a long drift tube was used as a dispersive element. Simulations were performed with different voltage settings according to the fixed relations in Eq. 3.4 and Eq. 3.6. The voltages used on the DT to study how large masses was accepted without any overlap for certain kinetic energies are -2000 kV, -4000 kV and -6000 kV. The result is plotted in Fig. 3.3 with logarithmic axes. It is rather interesting that

the function follows a linear relationship with almost no deviation. From the plot one can deduce that for molecular fragments that are typically a few ten a.m.u., energies up to about 10 eV can be resolved, which indeed is the typical energy released from the dissociation of a small molecule. Breakup of clusters can result in much larger fragments, often a few 100 a.m.u. Assuming that KER is low so that their velocity is dominated by thermal energy of a few meV, than these large fragments can be resolved.

3.1.4 Detector system

All components of the MCP delay-line detector system were purchased from RoentDek. The following section describes the link between the components and their operation.

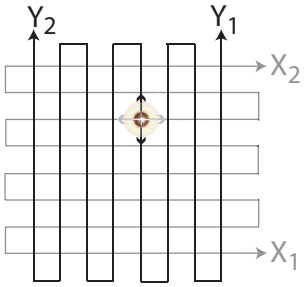

Figure 3.4: Schematic diagram of the delay-line anode. An ion arrival at the multichannel plates will be amplified into an electron cloud that is collected by the two orthogonal wire sets. In each wire, the electron cloud induces two current pulses that travel to the two ends of the wire sets. The difference in arrival time of the two pulses encodes the position and the average encodes the flight time.

Micro Channel Plate Detector and Anode

The MCP detector combined with delay-line anode (DLD80) is a high resolution timing and imaging device for detection of cations at high rates making it suitable for multiple coincidence measurements in momentum space. The detector consists of two MCPs with an active diameter of 80 mm in chevron configuration and a delay-line anode for position readout. The delay-line anode has two orthogonal sets of wires, where each set is composed of a signal wire and a reference wire. A maximum potential difference of 2400 V can be applied over the MCP. For new detectors, 2000 V is sufficient for a good signal to be generated, but as the detector ages, the voltage must be increased. The signal and reference wires were at 300 and 250 V, respectively, so that electrons will be preferentially collected by the signal wires.

The operation principle is illustrated in Fig. 3.4. When an ion hits the detector, an electron-burst is created that, at the corresponding position of the delay-line, induces a signal that travels in both directions with a speed close to that of light in vacuum. A perpendicular signal speed $v_\perp$ can be defined from the pitch of one wire loop (160 mm long and 1 mm wide) and the time it takes for a signal to propagate through the loop

$$v_\perp \simeq 3 \cdot 10^8 \frac{\mathrm{m}}{\mathrm{s}} \frac{1\mathrm{mm}}{160\mathrm{mm}} \simeq 0.95 \frac{\mathrm{mm}}{\mathrm{ns}}. \tag{3.7}$$

The position (X, Y) of a detected ion is related to the signal arrival time difference at the ends for each delay-line, independently for the two dimensions.

$$\begin{bmatrix} X \\ Y \end{bmatrix} = \begin{bmatrix} k_X \cdot v_\perp (X_2 - X_1) \\ k_Y \cdot v_\perp (Y_2 - Y_1) \end{bmatrix}, \tag{3.8}$$

where k_X and k_Y are two correction constants that are $\simeq 1$, but not necessarily identical. The ions flight-time coordinate T can be taken from the MCP backside signal, or alternatively as the meanvalue of the four position signals $T = \frac{1}{4}(X_1 + X_2 + Y_1 + Y_2)$. The three Cartesian coordinates is a dataset that contains the ions total kinematic information from which the linear momentum vector can be derived.

Electrical feedthrough
To collect the four differential signals and apply voltages on the detector, a flange (CF35) with a 12-pin-feed-through is used. It connects the in-vacuum cables with the accompanying air-side transmission plug (FT12-TP). For the delay-line signals, the plug provides adequate RC decoupling and transformer circuits to turn it into single-line 50Ω impedance signals. 50Ω is an often used standard since it has been found to be the best compromise between signal loss and high voltage that can be applied. Our applied voltages are given in table 3.1. To avoid electrical discharge between two electrodes in vacuum, they must be separated with 1000 V/mm. The voltage applied on the MCP front side is -2000 V, so care must taken to mount it slightly more than 2 mm from the grounded DT.

Table 3.1: Voltages, recommended by the manufacturer, applied on the detector through the FT12-TP. Over the MCP, a potential difference of about 2000 V is sufficient. The signal and reference wires are at 300 and 250 V, respectively, so that electrons will be preferentially collected by the signal wires.

MCP front	-2000 V
MCP back	0 V
Anode holder	0 V
Reference wire	+250 V
Signal wire	+300 V

Signal amplification and discrimination
The readout of the MCP and DLD80 signals requires circuits for amplification and time-discrimination. To produce NIM signals with a very high time precision for the time-to-digital converter (TDC), an especially designed ATR19 module was used. It hosts eighth independent differential timing and constant fraction discrimination (CFD) channels.

Time to digital converter
The six NIM signals (start, stop, X_1, X_2, Y_1, Y_2) are input to a time-to-digital converter TDC8HP (RoentDek). The TDC8HP is a PCI card that can be mounted in any x32 Bit system computer with a Windows OS. It features eight NIM compatible input connectors with 25 ps sampling rate and a typical deadtime between multiple hits on one channel of approximately 5 ns. During the deadtime, the TDC is blind for additional stop signals, with the consequence that for double coincidences where ions have same $\frac{m}{q}$ ratio, the sample that we measure is not representative of the actual distribution.

3.2 Experimental setup

The measurements were performed at Beamline I411 at MAX-lab in Lund, Sweden [62, 63]. During the experiment, the sample gas pressure in the apparatus chamber was kept at $5 \cdot 10^{-6}$ mbar, while the pressure in the monochromator chamber was $1 \cdot 10^{-9}$ mbar. The TOF axis is mounted at 90 degrees with respect to the horizontal polarization axis.

The analysis of photo-ions is performed with the TDC by using the electron signal as a start and multiple ion signals as stops. The TDC is interfaced with a computer program installed on a PC via a dedicated software module, and the $3D$ coincidence data of one electron with n ions are recorded, referred to hereafter as a PE(PI)^{n}CO (*PhotoElectron-n-PhotoIon-COincidence*) spectra, with the capacity of detecting up five ions in coincidence for each electron.

The main challenge in this experiment is the simultaneous detection of two or more products created in the same photoionization event, so to reduce the number of false coincidences, we must not exceed a certain count rate, λ. To estimate λ, we assume a model where the core ionizations occur according to a Poisson process, with the probability function

$$f(k) = \frac{e^{-\lambda t}(\lambda t)^k}{k!} \tag{3.9}$$

where k is the number of ionized molecules per time interval t, where the TDC-card is blind to new electrons impinging on the detector, typically 10 μs. If we want these false coincidences to be less then one percent of the total yield, it is easy to calculate from Eq. 3.9 that $f(0) + f(1) \geq 0.99$ gives $\lambda < 10^4$ Hz. We measure λ as the count rate at the electron MCP, and then regulate it by adjusting the gas flow and the brilliance. The false coincidences that still appear can be subtracted from the raw data by implementing a strategy developed by Frasinski *et al.* [64].

The detection efficiency is a product of several factors such as the open area ratio of the grids ($\sim 80\%$) and the probability to generate a signal from the MCP to the anodes that, according to the manufacturer, is $\sim 40\%$ and $\sim 60\%$ for ions and electrons respectively [65]. Taking this into consideration, we estimate a total efficiency of $\sim 20\%$ for ions, and $\sim 80\%$ for detecting one out of two electrons. So for example, a process leading to three cations will only be completely detected with the probability $0.2^3 \cdot 0.8 = 0.6\%$, while it is much more likely to detect only two of the ions, $3 \cdot 0.2^2 \cdot (1-0.2) \cdot 0.8 = 7.7\%$, or even more so, just one ion $3 \cdot 0.2 \cdot (1-0.2)^2 \cdot 0.8 = 31\%$. This low efficiency is a major problem in the analysis for those events where not all fragments are collected, making it hard to get a conclusive picture of the dissociation channels.

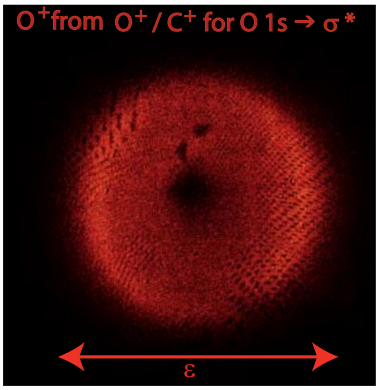

Figure 3.5: Detector image of O^+ from the two body breakup of carbon monoxide dication to C^+/O^+ after core excitation to O $1s^{-1}\sigma^*$ state. The alignment in the core excited state is retained in the photo fragments.

3.3 Data files

For data treatment, a computer program equipped with a graphical user interface was developed by me in the MATLAB-environment, named ANACONDA an acronym for "analysis of coincidence data". The interface provides the user with an intuitive way of selecting subsets of the $3n$ dimensional time-position space and presenting it from arbitrary projections in figures of publishable quality. Additionally, it is capable of transforming data into linear momentum coordinates, which is crucial in order to probe the dissociation dynamics.

Table 3.2: Single-coincidences are partitioned into three smaller files, one for each dimension. Double-coincidences into six files, etc.

	Single	**Double**		**Triple**		
	1^{st} ion	1^{st} ion	2^{nd} ion	1^{st} ion	2^{nd} ion	3^{rd} ion
T	`File1T1`	`File2T1`	`File2T2`	`File3T1`	`File3T2`	`File3T3`
X	`File1X1`	`File2X1`	`File2X2`	`File3X1`	`File3X2`	`File3X3`
Y	`File1Y1`	`File2Y1`	`File2Y2`	`File3Y1`	`File3Y2`	`File3Y3`

CoboldPC acquisition software from RoentDek was used for operation and data gathering from the delay-line detector. Due to the low detection efficiency for multiple coincidences, for sufficient statistics to be gathered, it is essential to collect a lot of data, typically several millions of events. Data storage and handling constitutes a difficulty. This was solved by writing a routine that produces the most often used data subsets and parameters to be saved as a number of small easily accessible binary files. The advantage of this approach is that only necessary data is loaded into memory, thereby significantly reducing the processing time. For each experiment single coincidences are partitioned into three files for X, Y and T. Double coincidences are partitioned in the same way into six files, and so on until quintuple coincidences that produces 15 files. See table 3.2. The resolution of this dataset is the maximum 0.1 mm×0.1 mm×25 ps. For a particular ion the coordinates (X,Y,T) are stored as `(int16,int16,uint32)`. Depending on what variable-correlations that are to be studied, only that particular combination is loaded into the RAM. A demonstration is given in Fig. 3.5, where we see O^+ that comes in coincidence with C^+ from carbon monoxide that has been core-excited to the O $1s^{-1}\sigma^*$ state. This is a $\Sigma \rightarrow \Sigma$ transition so the density is mostly aligned parallel to $\vec{\epsilon}$. To plot this data, the program in the first step loads the files `File2T1` and `File2T2` to define temporal constraints, than a filter is applied that removes all data outside the desired time-window. In the second step it loads `File2X2` and `File2Y2`, than a histogram is produced from the (X,Y) coordinates of the second ion. The histogram represents the detector-image in Fig. 3.5. When one observe the image closely, small dark spots can be distinguished, whom are related to the MCP pattern. An even higher sampling rate would thus not mean any improvement of resolution since here the holes in the MCP constitute the constraining factor. Also a couple of larger dark areas are visible and are due to poorer transmission efficiency in those spots on the MCP.

3.4 C_{60} evaporation oven

The momentum imaging spectrometer is limited to the analysis of gas-phase substances. Investigations of solids or liquids must be proceeded by evaporation of the sample. For the purpose of measuring the dissociation dynamics of C_{60} fullerenes, an evaporation source was developed. The source is a resistively heated effusive sublimation source, similar to what was used in Ref. [66, 67, 68]. The commercial fullerene powder, with a purity of 99.95% was heated in an oven to $600°C$ and the

fullerene vapor effuses. To minimize the fullerenes thermal energy, argon that was cooled by liquid nitrogen was used as a seeding gas that pushes C_{60} through the skimmer and to the center of the extraction zone of the spectrometer, where the interaction with the synchrotron radiation takes place. The heating element is a Thermocoax cold end resistive heating filament that is wrapped around the source volume [69]. A thermo-couple device is connected to the oven in order to measure the temperature.

Chapter 4

Results and Data Analysis

The linear-momentum imaging spectrometer gives us a kinematically complete description of charged fragment's trajectories after a multi-body breakup, from which nuclear motion and dissociation channels can be deduced. However, the detection of N ions in coincidence generates highly correlated data in a $3N$-dimensional Euclidean space, that is not trivial to disentangle. The problem offers a challenge regarding the data-treatment, where the objective is to extract relevant parameters that do not overwhelm us with information, but still contain everything of interest. This chapter is devoted to descriptions of a number of techniques for presentation and analysis of data.

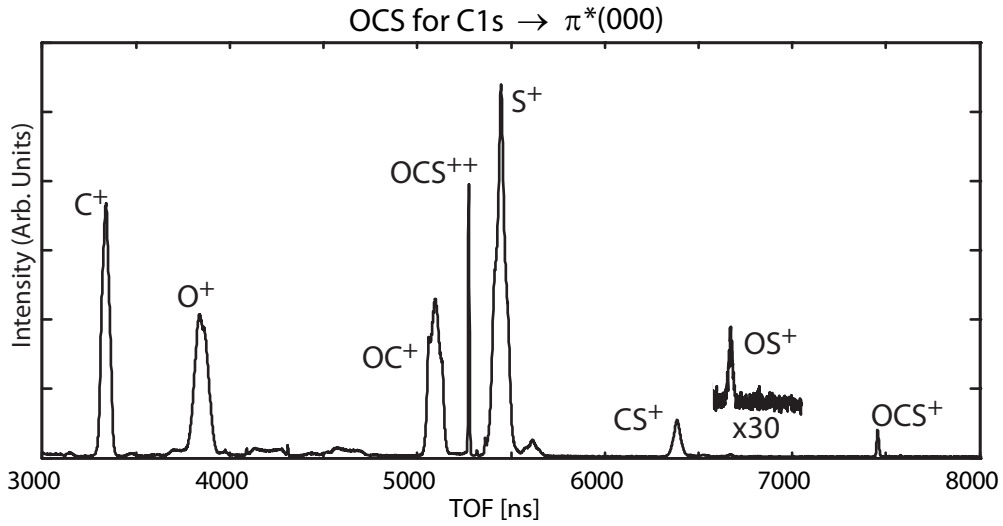

Figure 4.1: Time of flight plot of ionic fragments produced from dissociation of OCS excited to the C1s-$\pi^*(000)$ state.

4.1 Time and space coordinates

Regarding the ion's position data, a more natural choice of coordinate system than the Cartesian (X, Y), is the polar system where each point is given as a radius and angle (R, Θ). R is related to

the fragments KER, and Θ reveals the molecular alignment in the extraction region before breakup. The raw data from one ion is therefore most suitably presented with the cylindrical coordinates (T, R, Θ) where T is the ions flight-time.

4.1.1 TOF

Much information of relevance for the analysis can be found in the time of flight data alone. An example of a TOF plot is given in Fig. 4.1. It shows cationic fragments produced by dissociation of OCS prepared in the C1s$^{-1}\pi^*$(000) state. Only single coincidences are included, that is stable states or dissociative states that lead to only one charged fragment. With Eq. 3.5 each peak can be transformed into its $\frac{m}{q}$-ratio and thereby be identified. The small peak to the right of S^+ is the isotope $^{34}S^+$ that constitutes 4% of the total intensity ($^{32}S^+$ has 95%). Peak areas reveal the probability for certain dissociation pathways to exist. As an example the three diatomic fragments are studied. OC^+ registers more counts then CS^+ which indicates that for dissociative cationic states, the OC bond is stronger than the CS bond. A small yield of the more exotic fragment OS^+ was also detected at the C1s$\rightarrow \pi^*$ resonance. Existence of this fragment is evidence that the trans-bending motion can lead to isomerization. Indeed a pathway to the isomer COS was predicted from calculations by Brites *et al.* who showed that excitation to the C1s$^{-1}\pi^*$ state induces a Renner-Teller splitting, whereof in the bent state, a new bond can be created between the terminal atoms, and the original bonds are severed [70].

One striking feature is that the peaks for the parent ion, OCS^+ and OCS^{++}, are much narrower than peaks resulting from fragmentation. This is due to the kinetic energy released in the dissociation process. The larger KER, the larger is the deviation in TOF. The parent ions peak width thus only reflect the overall instrumental line broadening, that for OCS^{++} is 5 ns full width half maximum. Hence from the peak width, one can extract information about KER. More about this can be found in section 4.2.

4.1.2 TOF correlation plots

Time-correlation of collected PE(PI)^{n}CO-data is presented in a $2D$ histogram where the bins are functions of the faster time, T_A, and the slower time, T_B. Since these times are strongly dependent on the linear momentum, some correlation can be expected for this data, and it is therefore referred to as a *regression* spectrum that in many cases is characterized by a covariance-matrix and a slope [71].

However, the geometrical properties of this regression do indeed contain information about the dissociation dynamics, such as *Kinetic Energy Released* (KER), dissociation sequence and linear momentum vector of ejected fragments. To understand the meaning of the slope, one has to consider how the extraction field voltage affects the ionized fragments immediately after dissociation. This can be done by imagining two identical ions formed at the same position with the same speed but with velocities directed opposite to each other along the spectrometer axis. The ion moving away from the detector will, due to the electric field, turn around and after a time, ΔT, again pass the extraction plane, similar to a ball thrown up in the air. One can with basic classical mechanics derive the relation

$$\Delta T = \frac{2 \cdot p^Z}{q \cdot E_{ER}} \tag{4.1}$$

where p^Z is the ion's linear momentum vector component along the spectrometer axis and q is the charge, E_{ER} is the extraction regions electric field. The striking simplicity of this equation is attributed to the fact that neither the length of, nor applied voltage over the AR and DT has any impact on the time deviation. This means that the slope, $S_{B/A}$, resulting from coincidences

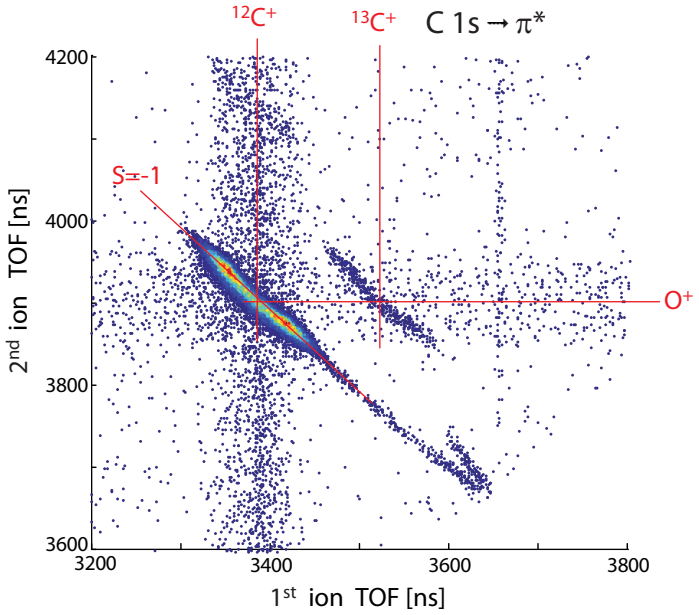

Figure 4.2: PEPIPICO map of resulting fragments from carbon monoxide core excited to the C 1sπ* state. The two most abundant carbon isotopes can be seen. The tail evidences a metastable dissociation pathway.

between the two ions is

$$S_{B/A} = \frac{q_A \cdot p_B^Z}{q_B \cdot p_A^Z} \tag{4.2}$$

where the indices A and B correspond to T_A and T_B, respectively. When the end product is two cations, because of conservation of linear momentum, $p_A^Z + p_B^Z \equiv 0$, the slope always has to be $-\frac{q_A}{q_B}$. So for two identical charges, exact anti-correlation is the result. To determine the slopes of the data, the *Least Square Method* turned out to be unreliable due to false coincidences. Furthermore, the precision of the result depends on the relative weighting of the flight times whose error is proportional to the total flight time. If the times in each ion pair are given equal weights, the error estimation might be incorrect. So instead, the slope and error for each regression, have been estimated manually.

Fig. 4.2 presents C^+/O^+ double-coincidences from CO after excitation to the C $1s^{-1}\pi^*$ state. The first ion to hit the detector is C^+, due to its smaller $\frac{m}{q}$ ratio, and the second is O^+. On the right hand side of the main peak is a weaker peak that is the $^{13}C^+$ isotope with a natural abundance of 1.1%. Indeed, the slopes are very close to -1, however the regression is not perfectly aligned along the -1 diagonal. This deviation can be explained with the inhomogeneous electric field due to the focusing lens, and must be compensated when transforming raw data into linear momentum coordinates. This will be explained in section 4.2.1. In Fig. 4.2 also a tail can be seen that starts at the lower right hand side of the regression and continues to the point in the diagonal where the TOF of the first ion is the same as that of the second ion. This feature is known to be due to metastable dissociation of the carbon monoxide dication [2, 12]. The potential surface has a shallow well where the wave packet can remain trapped for several vibrational cycles as was illustrated in Fig. 2.1, during which the dication accelerates through the electric field. At some point the wave packet will due to the thin potential barrier tunnel out and the dication will dissociate to C^+/O^+.If breakup takes place after the dication has entered the drift tube, no additional acceleration will be gained, so the fragments will continue through the spectrometer with the same velocity and hit

the detector simultaneously with the same TOF as the CO^{2+} fragment. In the area where the tail intersects the diagonal so that TOF(C^+) ≈TOF(O^+), the intensity is relatively high suggesting that many CO^{2+} fragments survive past the AR. From the length of the tail the dication lifetime can be estimated. Here it is found to be at least a few hundred ns.

The example in Fig. 4.2 furthermore illustrates the contribution of false coincidences as broad vertical and horizontal lines overlapping the regression $^{12}C^+/O^+$. Vertical lines arise if after an ionization event, fragmentation occurs to $e^-/C^+/O$. The electron triggers a start signal and opens a time window of a few μs. The carbon ion stops the clock after it hits the detector, but within the same time window an ion from another ionization event also arrives at the detector and produces a second stop, so the event erroneously becomes registered as a double coincidence instead of a single coincidence. The second ion has no correlation to either the electron or C^+, which explains the uniform vertical distribution. Horizontal lines are explained analogously, but instead it is the first ion that comes from an unrelated ionization. A third possibility of false coincidences, that however was not encountered in this spectra, is a double ionization that fragments into $2e^-/C^+/O^+$, where both ions are detected but the start signal comes from another ionization. Than the time difference between ions will remain constant, but the whole regression will be shifted in absolute time, so that a distribution can be seen along the diagonal line +1. The impact of false coincidences is a less reliable spectra, so minimization of their contribution is essential which is achieved with a low count rate as was explained in Sec. 3.2.

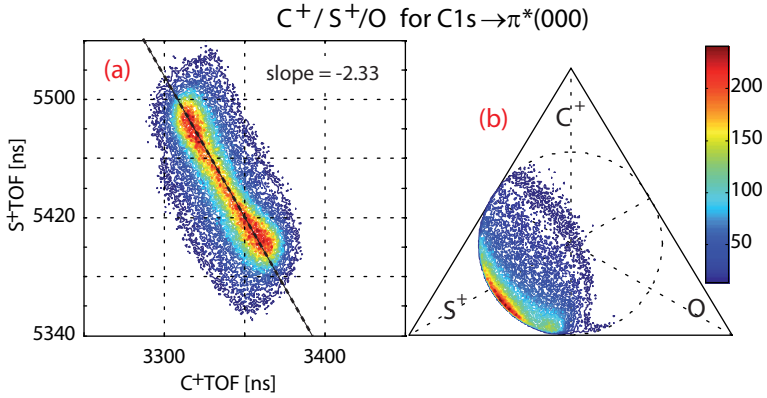

Figure 4.3: Dissociation of OCS dication into C^+/S^+. (a) The slope tells us that the dissociation is sequential where S^+ is the first fragment to be ejected. (b) The Dalitz plot confirms this pathway, suggesting that the Dalitz plot is a successful method for analysis of three-body breakups.

Spectra resulting from dissociations involving three or more final fragments are not as easy to analyze as the two-body case. However, since previous generations of Wiley-McLaren mass-spectrometers were not equipped with position sensitive detectors, the time correlation plots posed the limit of their capacity, a number of techniques have been developed to extract information. In the paper [72] by Simon *et al.*, a theoretical foundation was given that explains various regression spectra for three and four body fragmentation in detail as functions of mass, charge and excited state lifetime. These regressions were all confirmed with Monte-Carlo simulations developed by Eland [45].

To illustrate this with an example, measurements have been carried out on the OCS molecule at the C1s→ $\pi^*(000)$ resonance. In the ground state this has a linear configuration with oxygen and sulfur as terminal atoms so that it belongs to the $C_{\infty v}$ point-group. Fig. 4.3(a) presents data from the double coincidence channel C^+/S^+ in a Time Of Flight (TOF) correlation plot, where the regression has the slope $S_{S^+/C^+} \approx -2.33$. This slope can be explained with a sequential

dissociation process where the primary ejected fragment is S^+ with momentum $-p^Z_{S+} = p^Z_{CO^+}$. After the two ions are out of reach for Coulomb interaction, OC^+ breaks into C^+ and O, where C^+ receives the momentum $p^Z_{C+} = \frac{m_{C+}}{m_{OC+}} p^Z_{OC^+}$. The known values of the masses, produced the relation $p^Z_{S+} = -2.33 \cdot p^Z_{C+}$, that with Eq. 4.2 gives us the correct slope [36, 73].

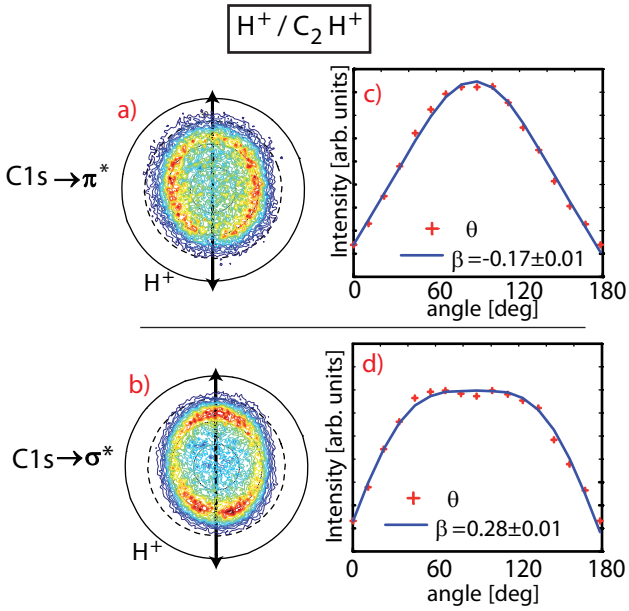

Figure 4.4: Experimental data on the H^+/C_2H^+ two-body dissociation channel. The polar plots show the location of the H^+ ions for: (a) the C $1s \rightarrow \pi^*$ resonance at 285.85 eV and (b) at 311 eV, which corresponds to the C $1s \rightarrow \sigma^*$ resonance. In the lower half of (b) an intensity anomaly can be seen intersecting $\vec{\epsilon}$, that is due to the field distortion from the injection needle. The direction of the polarization vector is shown in the plots. The β-parameter reduces the spherical angle distribution to one numerical value. (c) and (d) shows histograms of the zenith angular distribution, θ, with which β has been estimated.

4.1.3 Angular distribution

The image registered on the delay line detector (DLD80) reveals further information. The radius reflects KER, while the angular distribution of ejected fragments gives the alignment of the molecule before Auger decay [74, 75, 20]. As an illustrative example one can look at the deprotonation of the Ethyne dication, H^+/CCH^+. Fig. 4.4 (a) presents data for H^+ from this pathway produced at the C1s$\rightarrow$ π^* resonance. The arrows indicate the direction of the polarization vector. This is a $\Sigma \rightarrow \Pi$ transition meaning that the initial distribution is expected to be perpendicular to the polarization. It appears that the alignment is preserved, since the density maximums can be found at the opposite sides of $\vec{\epsilon}$. Because of conservation of momentum, the angular distribution of the other fragment (CCH^+), does not provide any additional information and has therefore been omitted. Fig. 4.4 (b) presents data for H^+ from this pathway produced by the C1s$\rightarrow$ σ^* that is a $\Sigma \rightarrow \Sigma$ transition meaning that the initial distribution is expected to be parallel to the polarization. Also here the data is in agreement with the expected alignment. To compensate for possible offset on the detector, the mother ion $C_2H_2^+$ was selected, that has no significant kinetic energy resulting in a tiny spot in the center of the detector image. The center of the spot is defined as the detector-center.

4.2 Linear momentum coordinates

The examples given above demonstrate that a lot of information is waiting to be gathered in this uncharted field of reaction dynamics. This advantageous condition, however, brings up the question of how to systematically define a standardized method to characterize dissociation processes.

The momentum imaging spectrometer provides us with complete kinematic information. However what is interesting in order to understand the dissociation mechanism is not only the end-product's momentum and KER, but also how these parameters are correlated with respect to each other for fragments in coincidence. Due to the entangled multidimensional nature of this task, it is essential to diagonalize the problem so that a reduction of dimensions can be carried out without losing vital information. For three body breakups, there are two methods commonly used to accomplish the objective of presenting data in standardized $2D$-histograms, namely: *Dalitz plots* and *Newton diagrams,* described in section 4.2.2 and 4.2.3 [76, 77, 78, 79]. The information that is lost in these two presentations is the photoions angular distribution with respect to the polarization vector. This can be described with the β-parameter, explained in section 4.2.4.

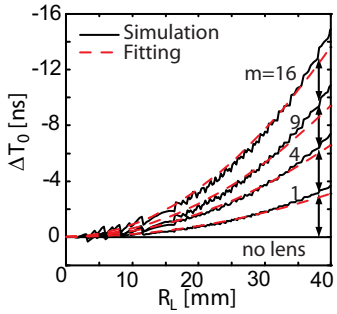

Figure 4.5: Deviation in TOF with lens activated as a function of the radius on the detector where the ions hit. ΔT_0 has a quadratic dependence on R_L and a linear dependence on T_0. See text for details.

4.2.1 Data transformation

A crucial part of the data treatment is the translation of raw-data into a linear momentum space. The electrostatic lens creates a potential "bubble" in the otherwise field-free region, that imposes a deviation on the charged particles trajectories. The complexity of the problem forces us to abandon the derivation of an analytical expression, and resort to numerical computer simulations. The commercially available software package SimIon 7.0 was utilized [59]. It is a versatile platform, developed for various types of charged particle optics systems, such as high precision ray tracing of cations in electrostatic fields. A powerful feature of SimIon is its support for importing `.stl`-files from the CAD program used to design the spectrometer, and interpreting the geometry as electrodes, so a new model of the spectrometer is not required.

The field potential at any point within an electrostatic lens can be found by solving the Laplace equation with the electrodes acting as boundary conditions. The interface allows the user to select masses, charges and initial momentum vectors for fragments. Ion trajectories are then calculated through the generated field and the coordinates where they impinge the detector are registered with 100 μm resolution.

It is desirable to minimize the amount of computer calculations to be performed. A semi-analytical approach is therefor used. Here cylindrical coordinates have an advantage over the Cartesian system, since the polar angle, Θ, remains unaffected during the transformation to the zenith angle θ, thereby a dimension reduction is accomplished and only the TOF and radial dimensions are related to the kinetic energy.

TOF transformation
It is useful to start with an analytical approach where the influence of field inhomogeneities are not taken into consideration. Transformation of flight-time into momentum is most efficiently done with Eq. 4.1, so that momentum in Z-direction becomes $p^Z = 0.5 \cdot \Delta T \cdot q \cdot E_{ER}$, where what is relevant is not the actual TOF, but only the deviation, ΔT. The time deviation is given as the difference between the time an ion spends in the flight tube, T, and the time it would spend if it had zero momentum in the Z-axis, T_0. An estimate of T_0 can be made from TOF in Eq. 3.5, so $\Delta T = T - a - b \cdot \sqrt{\frac{m}{q}}$, where a and b are found experimentally.

Activation of lenses causes an inhomogeneous field where ΔT also depends on a contribution from the ions radial coordinate, R_L and is proportional to the actual time, T_L it spends in the spectrometer, which makes conversion into momentum coordinates a significantly tougher challenge. Without lenses, when there is no momentum in the spectrometer axis, ΔT must be zero. For applied lenses, that is not necessarily the case, so a simulated time deviation, ΔT_0 is defined and the momentum in the spectrometer axis is set as zero

$$\Delta T_0 \mid_{p^z=0} = f^T(T_L, R_L) \tag{4.3}$$

Trajectories for cations have been simulated with different masses that are ejected perpendicular to the spectrometer axis with different kinetic energy. In Fig. 4.5(a) the correlation between the radius where the ions hit the detector, R_L, and their deviation ΔT_0 in TOF is plotted. For all masses, it is possible to approximate accurately ΔT_0 as a function of R_L with a second order polynomial. For radii's up to 40 mm, ΔT_0 never deviates with more than 0.7 ns, which is sufficient accuracy. The error made corresponds typically for small molecules to a kinetic energy of ~ 0.05 eV which is about the same as the thermal energy and thus insignificant. For large molecules fragment kinetic energies are usually relatively small with a radius that do not extend more than 20 mm on the detector. To estimate the effect of the nominal flight time T_0 dependence, ions with masses from a quadratic distribution $m \in \{1, 4, 9, 16\}$, which is equivalent to a linear deviation in T_0 have been selected. Indeed, for any given value R, it is seen in the figure that ΔT_0 changes with a linear dependence on T_0. If assuming that the radial contribution has no dependence on p^Z, it leads to the relation

$$\Delta T_L \approx \Delta T + \Delta T_0 = \frac{2 \cdot p^Z}{q \cdot E_{ER}} + K^T \cdot T_0 \cdot R^2 \tag{4.4}$$

from which p^Z can be derived using eq. 4.1 and the constant K^T being estimated with a least square method. Similar relation was found by Lebech *et al.* [80].

Radius transformation
Assuming that no force affects the ions velocity in the direction perpendicular to the spectrometer axis, then the radial distribution is the particles radial velocity multiplied with the time they spend in the spectrometer, $R = v^R \cdot (T_0 + \Delta T)$. Kinetic energy is described as $E^R = 0.5 \cdot m \cdot {v^R}^2$, so the radial dependency on the fragments perpendicular energy is

$$R = \sqrt{\frac{2E^R}{m}} \cdot (T_0 + \Delta T). \tag{4.5}$$

From Eq. 3.5, if redefining the time scale so that $a = 0$, the relation $\frac{T_0}{\sqrt{m}} = \frac{b}{\sqrt{q}}$, gives the analytical expression

$$R = b \cdot \sqrt{\frac{2E^R}{q}} \cdot (1 + \frac{\Delta T}{T_0}). \tag{4.6}$$

where it can be seen that the radial distribution is the same for all ions with the same charge. The mass dependence have thus been replaced with charge dependence which reduces the amount

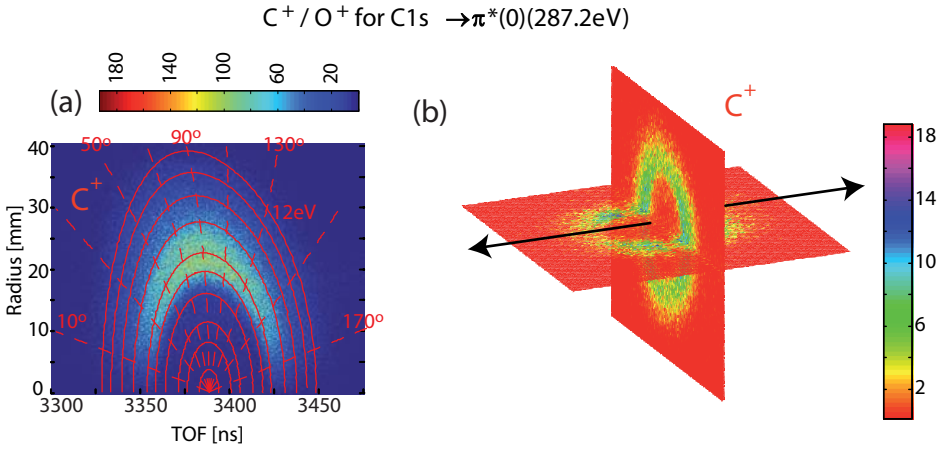

Figure 4.6: (a) A correlation plot between ions TOF and the detector radius where they hit provides information of the fragments kinetic energy. The larger the crescent shape is, the more energy is released. The simulation curves agrees well with the experimental data. (b) A two-plane cross-section of momentum sphere of the fragment C^+ from the C^+/O^+ pathway in CO after core excitation to the $C1s^{-1}\pi^{*1}$ state. Clearly all the data are within a well defined region.

of mappings since usually only cations and dications must be considered. Because of the field inhomogeneity, Eq. 4.6 can however not describe the radial distribution correctly and must be replaced with a simulated distribution, R_L. If the time-deviation is set as zero, one get

$$R_L \mid_{\Delta T=0} = b\sqrt{\frac{2}{q}} \cdot f^R\left(\sqrt{E^R}\right) \tag{4.7}$$

Ion-trajectory simulations were performed with the relevant potential settings and it was found that R_L has a linear dependence on $\sqrt{E^R}$, thus $f^R\left(\sqrt{E^R}\right)$ can be approximated with the linear relation $K^R \cdot \sqrt{E^R}$. The time-deviation can be divided from both sides and becomes a correction factor

$$R_L\left(1+\frac{\Delta T}{T_0}\right)^{-1} = b\sqrt{\frac{2}{q}} \cdot K^R \cdot \sqrt{E^R} \tag{4.8}$$

A bijective mapping function is thus produced that takes into account the flight time dependence on the radial shift. For an ion with a certain mass, E^R can than be transformed to the radial momentum component p^R. A complete dataset (θ, p^R, p^Z) in cylindrical momentum space is thus created. It can be used to extract the measurable parameters such as kinetic energy given by

$$E_K = \frac{{p^R}^2}{2m} + \frac{{p^Z}^2}{2m}. \tag{4.9}$$

Example

Fig. 4.6(a) shows empirical data of C^+ that comes in coincidence with O^+ from carbon monoxide core excited to the C $1s^{-1}\pi^*$ state plotted as TOF/Radius correlation. The more energy that is released, the larger is the deviation both in time and in the radial distribution, so the size of the crescent-shape is a measure of the KER. The red curves are distributions, calculated according to the semi-analytical method that was described. Each dashed curve corresponds to a fixed elevation angle of the momentum vector with respect to the spectrometer axis, and each filled curve to a fixed KER value but different velocity vectors. The outermost curve represents 12 eV, the innermost 0.1 eV. It thus constitute a coordinate system in fragments KE and direction. Furthermore a

substantial asymmetry can be seen around T_0 that can be explained by the inhomogeneous electric field and also the fact that for the same KER, positive ΔT leads to larger radius than negative ΔT. A comparison between experimental and simulated data provides us with a transformation from the detector position and TOF to its corresponding momentum vector $\vec{p}$.

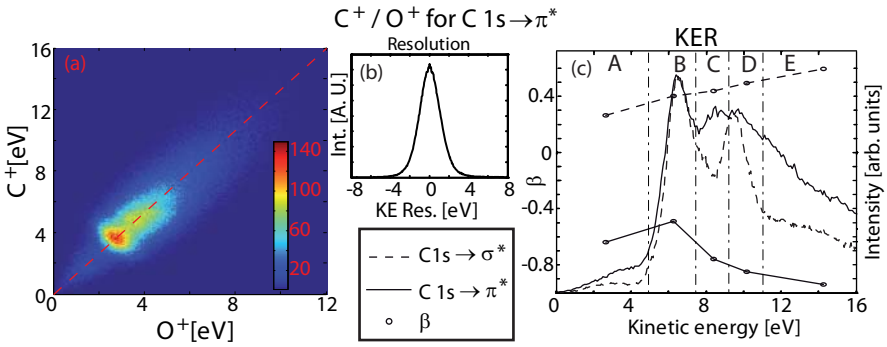

Figure 4.7: (a) Kinetic energy correlation for the C^+/O^+ ion pair from core-excited carbon monoxide. Each peak reflects a certain dissociation pathway. (b) The curve describes the energy resolution. (c) KER distribution. The multi peak structure makes this a suitable candidate for energy calibration.

The distribution of ejected fragments motivates a further transformation to the spherical coordinate system, (θ, ϕ, p), that is more intuitive. The azimuth, θ, and zenith, ϕ, angles gives the ions alignment in the extraction region before breakup, and therefore measures the anisotropy. p is the absolute value of the linear momentum, $|\vec{p}|$, and thus gives us the KER as $\frac{p^2}{2 \cdot m}$ for a fragment with mass m. Furthermore, p can be used to filter data since ion's from a particular pathway are located within a spherical region in momentum coordinates, so that everything outside of this region is either false coincidences or other fragments with same $\frac{m}{q}$ ratio. Fig. 4.6(b) shows a two-plane cross-section of momentum sphere of the fragment C^+ from the C^+/O^+ pathway in CO after core excitation to the $C1s^{-1}\pi^{*1}$ state. The arrow indicates the polarization vector. Clearly all the data are within a well defined region and also it is possible to see that the density is lower in the region close to $\vec{\epsilon}$ as is expected for this transition. Our aim is to probe dissociation dynamics during and after the photochemical process. To accomplish that, one must study fragments correlation. For two-body breakups, the two fragments linear momentum must be conserved, $p_{\vec{C^+}} = -p_{\vec{O^+}}$, leading to the relation $\frac{E_{C^+}}{m_{O^+}} = \frac{E_{O^+}}{m_{C^+}}$, along which ideally all data must be defined. Fig. 4.7(a) shows the corresponding KE correlation for O^+ and C^+ in coincidence. A few spots can be distinguished where indeed the distribution follows the calculated linear condition (dashed line). Each spot corresponds to a breakup from a particular final dissociative state of the dication to states of the cationic fragments. The deviation from the dashed line is a measure of the spectrometers overall resolution. An integration performed perpendicular to this line $\nu = \frac{E_{C^+}}{m_{O^+}} + \frac{E_{O^+}}{m_{C^+}}$

$$\int_{\nu=0}^{\infty} I(C^+, O^+) d\nu \tag{4.10}$$

is plotted in Fig. 4.7(b), where I is the intensity distribution. The full width half maximum is ~ 1.8 eV.

Regarding twobody breakups, other than the resolution, there is no loss of information by instead presenting KE data as a total KER histogram. In Fig. 4.7(c), the energies for each ion pair were summed after core excitation to both the C $1s^{-1}\pi^*$ and C $1s^{-1}\sigma^*$ states. The multi-peak structures makes this two-body breakup a suitable candidate for calibration of our transformation. The distribution agrees well with previously published results by Journel *et al.* [10]. Assignment

of peaks can be done by subtracting the binding energy of the repulsive molecule with that of the fragments electronic states, see schematic in Fig. 2.3. The most intense peak at 6.4 eV KER (region B) is attributed to the $(5\sigma 1\pi)^{-1}\ ^1\Pi$ final state at 41.8–43 eV binding energy region, that dissociates into the ground states of the cationic fragments $C^+(^2P)$+$O^+(^4S)$ at 36 eV above the neutral ground state. Again, assuming that the fragments are in their ground states, the other two peaks (region C and D) are mainly $(1\pi)^{-2}\ ^3\Sigma$ at 44.4 eV and $(4\sigma 5\sigma)^{-1}\ ^1\Sigma$ at 45.7 eV. These assignments agree with Journel *et al's.* [10]. The broad peak at ~ 3.5 eV (region A) was explained as a sequential process where Auger decay first populates repulsive states in CO^{+*} in he binding energy region 36–41 eV that dissociates into $C^+(^2P)$ and autoionizing $O^*(^3D,^3F,^3P)$ at 36.5 eV.

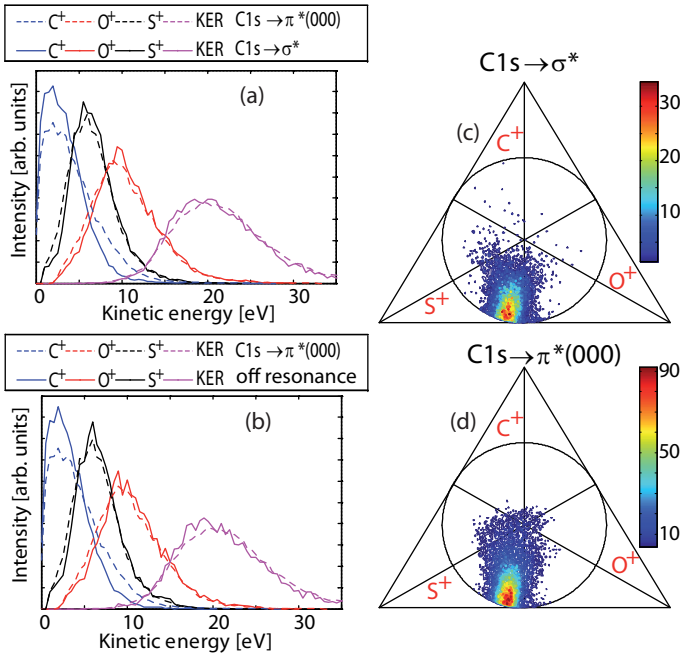

Figure 4.8: KER distribution at C1s→ π^* with (a) C1s→ σ^* and (b) off resonance are compared. The total KER displays no photon-energy dependence, but at $C1s^{-1}\pi^{1*}$ terminal fragments have more energy, while the central fragment gains less kinetic energy. In (c) and (d), by using Dalitz plots, the fragment energy ratios are compared. Decay from the $C1s^{-1}\pi^{1*}$ state, imports a larger fraction of energy to the C^+ fragment then from $C1s^{-1}\sigma^{1*}$. The uncorrelated distribution of the fragments in the Dalitz plots further suggests that the breakup is concerted (see text for details).

Fig. 4.8 gives an example of how the KER distribution can be used for analysis. Data for each fragment from the triple coincidence channel $C^+/O^+/S^+$, produced from core excitation to the states $C1s^{-1}\pi^{*1}$ (288.2 eV) are compared with (a) $C1s^{-1}\sigma^{*1}$ (311.5 eV) and (b) off resonance. Our measured total KER distributions display no significant difference, meaning that same final dissociative states are populated. However, the terminal ions O^+ and S^+ are slightly shifted to lower energies for C1s→ π^*, while C^+ has a rather significant shift to higher energies at this resonance. This behavior indicates that a bending motion is induced in the $C1s^{-1}\pi^*$ excited state.

4.2.2 Dalitz plots

Once the momentum coordinates are established, a more detailed data analysis can be initiated Regarding triple coincidences, if one only consider the correlation of the fragments KER and ignore their direction, the problem is reduced from nine to three dimensions. The normalized square of

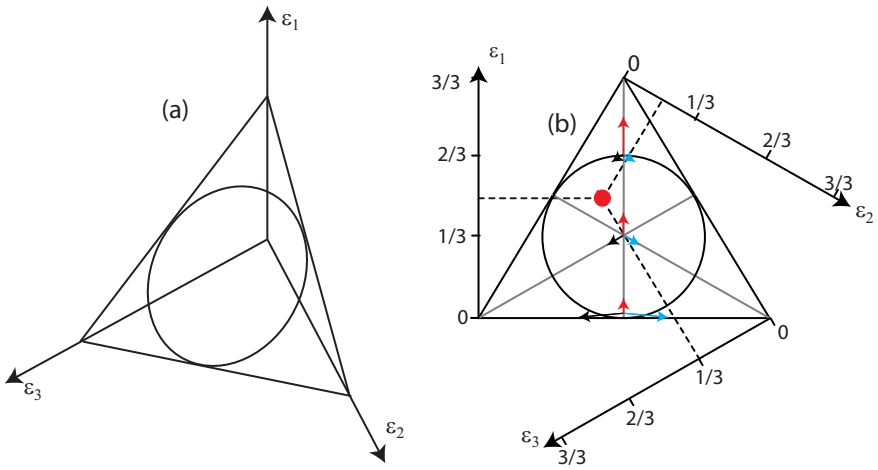

Figure 4.9: (a) The triangular plane defines the energetically allowed area in a three-dimensional Cartesian plot of fragment kinetic energies. The inscribe circle defines the kinematically allowed area. (b) General Dalitz plot. The tangent circle of radius 1/3 is inscribed in an equilateral triangle of unit height. Each point is determined from the values of the reduced kinetic energies ϵ_i of the three particles. Each Dalitz axis i is shown as a vector of unit length drawn from the center of one side of the triangle ($\epsilon_i = 0$) to the opposite vertex ($\epsilon_i = 1$). For any point in the circle the value of ϵ_i is given by the perpendicular projection of the point along axis i. The sum of the three ϵ_i equals one.

linear momentum ϵ_i of each ion i.

$$\epsilon_i = \frac{p_i^2}{\sum_{i=1}^{3} p_i^2} \tag{4.11}$$

is a dimensionless parameter that is related to the kinetic energy distribution between the three fragments. Due to the normalization, the condition:

$$\sum_i \epsilon_i \equiv 1 \tag{4.12}$$

imposes an energetic constraint on the energy triples to lie on a triangularly shaped plane intersecting the three energy axes $\epsilon_i = 1$ in the Cartesian coordinate system. There is an additional kinematic constraint based on the conservation of linear momentum:

$$\sum_i \vec{p}_i \equiv \vec{0} \tag{4.13}$$

that excludes regions impossible to reach, such as the coordinate (1,0,0) that would mean one fragment leaves with all the kinetic energy while the others have none. The latter constraint thereby limits the range to a circular area that touches the triangles sides, see Fig. 4.9 (a).

Since all the data is located in a plane, a suitable transformation van reduce one additional dimension so that finally the data can be described with only two coordinates

$$x_D = \frac{\epsilon_2 - \epsilon_3}{\sqrt{3}} \quad | \quad y_D = \epsilon_1 - \frac{1}{3}. \tag{4.14}$$

The remaining two dimensional dataset is called the Dalitz plot. The concept of Dalitz plots was originally developed to describe the three-body decay of a τ-meson into three identical π-mesons, and was later transferred to the investigation of chemical reactions [81, 82, 83, 84].

The Dalitz plot shows the ratio of KER for each fragmentation event as a single coordinate. The data is located within the circle of radius $\frac{1}{3}$ inscribed in the equilateral triangle. Each Dalitz

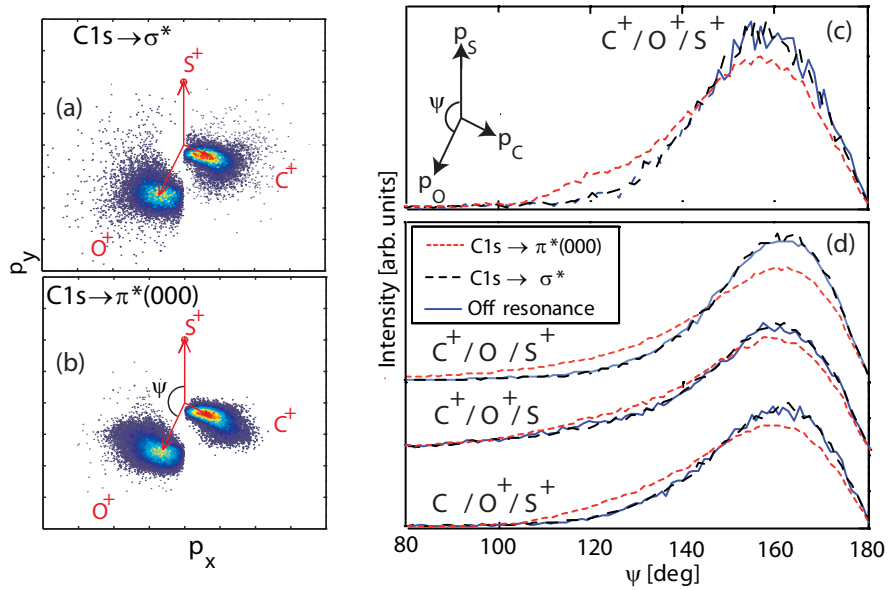

Figure 4.10: Newton diagrams for (a) $C1s^{-1}\sigma^{1*}$ and (b) $C1s^{-1}\pi^{1*}$. To compare angular correlations a histogram is plotted in (c) for both photon energies as well as off resonance. At $C1s^{-1}\pi^{1*}$ state smaller angles are reached. The same behaviour is seen for all three-body breakups (d), thus suggesting that bending is induced in the core-excited state.

axis i is a vector drawn from the center of one side to the opposite vertex. Energy normalization restricts all points to lie within the triangle of unit height, while conservation of momentum further restricts them to lie in the circle. For an arbitrary point the value of ϵ_i is given by the perpendicular projection along the Dalitz axis i. Thus the maximum possible value for ϵ_i is $\frac{2}{3}$, resulting with the other fragments receiving $\epsilon_j = \epsilon_k = \frac{1}{6}$ each, see Fig. 4.9 (a).

A three-body-breakup is a process that proceeds over a certain time-scale. Dalitz-plots are efficient tools in the investigation of dissociation dynamics. The remainder of this section will explain how to interpret the Dalitz plot density distribution for two cases:

After core-ionization, an Auger electron is emitted, whereupon two-body breakup can occur. It is possible that one cationic molecular fragment is dissociative, so it then undergoes a second breakup and auto-ionization. If the time between the bond-breaks is long enough for the fragments produced in the first step to escape Coulomb interaction before the second step, it is a sequential dissociation scheme that can be written as:

$$\begin{aligned} \mathrm{ABC} + \mathrm{h}\nu \quad &\rightarrow \mathrm{ABC}^{*2+} + \mathrm{e}^-_{photo} + \mathrm{e}^-_{Auger1} \\ &\rightarrow \mathrm{AB}^{*+} + \mathrm{C}^+ + \mathrm{e}^-_{photo} + \mathrm{e}^-_{Auger1} + \mathrm{KER}_1 \\ &\rightarrow \mathrm{A}^+ + \mathrm{B}^+ + \mathrm{C}^+ + \mathrm{e}^-_{photo} + \mathrm{e}^-_{Auger1} + \mathrm{e}^-_{Auger2} + \mathrm{KER}_1 + \mathrm{KER}_2, \end{aligned}$$

where KER_1 and KER_2 is the KER from the first and second bondbreak. It is evident that after the first breakup, the fragment C will have a constant fraction of the kinetic energy released in the first step. Since the breakup of AB does not affect C, no correlation is expected for ϵ between C and either A or B. A and B however, were produced simultaneously and ejected with opposite momentum vectors that are added to their initial linear momentum. This means that when A reaches its maximum momentum, B has its minimum and vice versa, so anti-correlation between ϵ_A and ϵ_B is expected. This is exactly what is seen in Fig. 4.3(b) where ϵ_{C^+} and ϵ_O are anti-correlated to each other but uncorrelated to ϵ_{S^+}. Here, the momentum of the neutral,

and therefore undetected, oxygen atom has been derived by assuming conservation of momentum, $-\vec{p_O} = \vec{p_{C^+}} + \vec{p_{S^+}}$. One can therefore use the Dalitz plot to confirm what was shown in section 4.1.2 with the TOF correlation plots: Namely that the C=S bond is the first to break, followed by secondary breakup of the OC^+ fragment.

A chain of Auger processes can produce a triply charged ion that is likely to undergo a concerted Coulomb explosion resulting in three charged fragments:

$$\begin{aligned} ABC + h\nu \quad &\rightarrow ABC^{3+} + e^-_{photo} + e^-_{Auger1} + e^-_{Auger2} \\ &\rightarrow A^+ + B^+ + C^+ + e^-_{photo} + e^-_{Auger1} + e^-_{Auger2} + KER \end{aligned}$$

The geometrical configuration is almost fixed, so the total KER is distributed between the three fragments with a certain ratio given to each of them. In the Dalitz plot we therefore expect to see a spot somewhere on the disc. In Fig. 4.8 (b,c), where $O^+/C^+/S^+$ triple coincidence from carbonyl sulfide is presented, this is exactly what we see. These figures also illustrate the phenomenon that we discovered in the KER distributions where C^+ receives a larger portion of the total energy for the $C1s^{-1}\pi^*$, than for the $C1s^{-1}\sigma^*$ state.

4.2.3 Newton diagram

Dalitz plots only provide us with information about the fragment's relative kinetic energy, but does not reveal anything about their direction in space. To accomplish that we use the Newton diagram that presents correlation of linear momentum [54, 85, 13, 86, 87].

Measurement of the momentum for triple-coincidences generates nine degrees of freedom. Representation of three vectors from a certain dissociation-event can however be done in one three-dimensional momentum space. Due to conservation of linear momentum (Eq. 4.13), the three vectors define a plane in this space, so a further dimension reduction can be performed.

When studying the vector correlation of the fragments produced in the three-body breakup, no consideration of their absolute magnitude or their orientation with respect to the polarization-axis of the light is necessary. Therefore we can rotate all vectors in such a way that they are in the plane of the paper and that one of them, for example $\vec{p_A}$, is directed vertically. All momenta are also normalized to the momentum of $\vec{p_A}$. The intensity for $\vec{p_B}$ and $\vec{p_C}$ is given as contour plots on a linear scale. In order to find the angle φ between two momentum vectors, the scalar product can be used:

$$\varphi_{A,B} = \arccos\left(\frac{\vec{p_A} \cdot \vec{p_B}}{|\vec{p_A}||\vec{p_B}|}\right) \tag{4.15}$$

The mathematical expression of scalar product is most easily defined in Cartesian coordinates, so here a transformation from cylindrical coordinates to (p^X, p^Y, p^Z) must be carried out. Newton diagrams thus give us information on the ion's relative magnitude and direction in space.

In Fig. 4.10(a,b), Newton diagrams have been produced for $C^+/O^+/S^+$ at the $C1s^{-1}\pi^*$ and $C1s^{-1}\sigma^*$ states. Considering what we saw in the Dalitz plots, we expect O^+ and S^+ to approach each other at the $C1s^{-1}\pi^*$ state, because the higher energy ratio for C^+ should be connected to a larger bending. To compare the Newton diagrams more easily we have plotted a histogram of the angle between O^+ and S^+ in Fig. 4.10(c). Clearly they reach smaller values at the $C1s^{-1}\pi^*$, which suggests that the bending motion takes place in that state. The fact that correlations between angles give the same information as the other data representations (KER, Dalitz and Newton) as an easily comparable and interpretable distribution, we continue our analysis by only studying angular correlations. To find more conclusive evidence that bending is induced by the core excitation rather than in one of the final states, we also investigate the other three body breakups. Fig. 4.10(d) presents angular correlations for the pathways of the dication where the neutral has been estimated by conservation of momentum. Just as for $C^+/O^+/S^+$, off and above resonance

distributions are identical while at the C1s$^{-1}\pi^{*1}$ state, smaller angles are always reached, which is evidence that the bending motion takes place in that state.

For purely sequential processes, Newton diagrams can be used to determine how KER is partitioned between the two dissociation steps. If fragment C is the first to be ejected, due to conservation of momentum, the measured value $\vec{p_C}$ directly reflects the energy released from the first step:

$$KER_1 = \frac{p_C^2}{2m_C} + \frac{p_C^2}{2(m_A + m_B)}. \tag{4.16}$$

The momentum of the particles, A and B, can be described as the vector addition of the momentum gained in the first and the second bond-break:

$$\vec{p_A} = \vec{p_{A_1}} + \vec{p_{A_2}} \quad | \quad \vec{p_B} = \vec{p_{B_1}} + \vec{p_{B_2}}, \tag{4.17}$$

where $\vec{p_A}$ and $\vec{p_B}$ are the measured values. $\vec{p_{A_1}}$ and $\vec{p_{B_1}}$ can be derived as:

$$\vec{p_{A_1}} = \frac{m_A}{m_A + m_B}\vec{p_C} \quad | \quad \vec{p_{B_1}} = \frac{m_B}{m_A + m_B}\vec{p_C}. \tag{4.18}$$

Thus we have the information required to retrieve the energy released also in the second step:

$$KER_2 = \frac{p_{A_2}^2}{2m_A} + \frac{p_{B_2}^2}{2m_B}. \tag{4.19}$$

4.2.4 β-parameter

The Newton and Dalitz plots reveal nothing about the fragment's angular distributions, but in the field of molecular dynamics, angular information is essential for the understanding of molecule-light interaction. As was shown in section 2.1.7, the normalized distribution over the zenith angle is $I_\theta(\theta) \propto \sin\theta[1 + \beta P_2(\cos\theta)]$. Since we collect complete fragment angular information, we have the possibility to extract the partial-ion-yield β-parameters that describe the anisotropy of all ionic fragments formed upon photodissociation. The data is transformed into linear momentum space in spherical coordinates, so that a histogram of θ can be plotted. β is then estimated with a least square fit of $I_\theta(\theta)$ to this histogram, thereby providing us with the recoil anisotropy [88]. A nonuniform detection efficiency of the detectors would influence the estimated anisotropy-parameter.

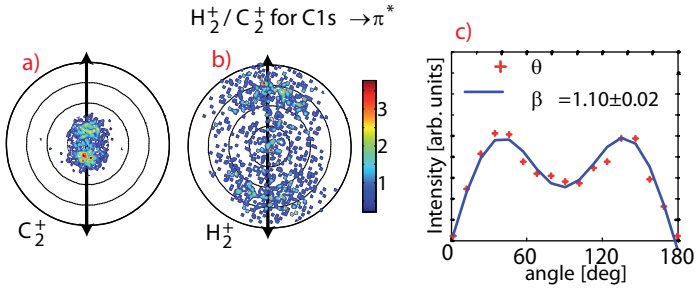

Figure 4.11: Experimental data on the H_2^+/C_2^+ two-body dissociation channel. (a) and (b) shows the location of the H_2^+ and C_2^+ ions for the C $1s \rightarrow \pi^*$ resonance at 285.85 eV. A histogram of their average angular distribution is plotted in (c) from which β has been extracted.

The ethyne deprotonation channel introduced in section 4.1.3 is used to illustrate the concept and usefulness of the β-parameter. Examples of real anisotropic distributions are presented in

Fig. 4.4 for the core-excitation $C1s \rightarrow \pi^*$ at 285.85 eV, a $\Sigma \rightarrow \Pi$ transition (c), and for the core-ionization $C1s \rightarrow \sigma^*$ at 311 eV, a $\Sigma \rightarrow \Sigma$ transition (d). θ has been estimated as the mean-value of the two ions. Error estimation of β was made with residual-analysis, so that the residuals do not deviate by more then 10% from their minimum value. The β values are in qualitative agreement with what is expected, but still far from totally anisotropic, suggesting that bending vibrations that distort the alignment have a significant impact on both the core-excited and ionized states.

Another two-body dissociation channel which results from hydrogen migration is the H_2^+ and C_2^+ pair. This pair is found almost exclusively at the C$1s^{-1}\pi^{*1}$ state, and shows a strong asymmetry along the direction of the polarization of the exciting radiation. The measured coincidence data at the C$1s^{-1}\pi^{*1}$ are presented in Fig. 4.11, where β is 1.1. This asymmetry is very different than the measurements of the C_2H^+/H^+ pair, where β was found to have the negative value -0.17. The positive β value estimated from the H_2^+/C_2^+ channel can be explained by the nuclear dynamics in the C $1s^{-1}\pi^{*1}$ state. The induced bending upon core-excitation can occur only in one direction, that of the polarization axis, so the photon absorption process can not be regarded as separate in this case. Instead, during excitation, photoabsorption triggers the nuclear motion where the corresponding transition dipole moment is perpendicular to the C-C bond and parallel to $\vec{\epsilon}$. By filtering the H_2^+/C_2^+ channel, we only monitor molecules undergoing a *cis* motion. The subsequent dissociation keeps the memory of this alignment, which is reflected in the intensity distribution of the H_2^+/C_2^+ fragments, parallel to the polarization vector, $\vec{\epsilon}$.

4.2.5 Data filters

With previous generations of ion-spectrometers, where only TOF data was available, different dissociation mechanisms resulting in the same final fragments could not be resolved. Access to complete kinematic information provides us with a solution since fragments kinetic energy and angular distribution are characteristic parameters that may be used to apply further filters and thereby separate various mechanisms.

Energy filter

Fig. 4.7(c) shows KER distribution for the two body breakup C^+/O^+ from core excited carbon monoxide. It is known that the C 1s$\rightarrow \pi^*$ is a pure $\Sigma \rightarrow \Pi$ transition that under the axial recoil approximation must give $\beta = -1$ [89]. A filter was applied and the anisotropy calculated in each of the five regions (A-E). For high KER values, especially region E, the axial recoil approximation seems to hold. For smaller energies however, a more isotropic distribution is evident. Especially region B where $\beta \approx -0.4$. The deviation from $\beta = -1$ can be explained with metastable states in the dication that allows it to rotate and thus loose information about its initial orientation before breakup [2]. Indeed, this is in agreement with the metastability that was evidenced in Sec. 4.1.2 and suggests that the $CO^{2+}(^1\Pi)$ electronic state (region B) contributes the most to the metastability.

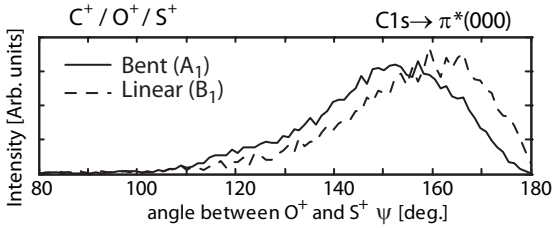

Figure 4.12: A histogram of the intensity as a function of bond angle (ψ) for the two RennerTeller components at the C $1s^{-1}\pi^*$ state. The events corresponding to the bent geometry and the linear geometry are compared.

Angle correlation filter
In Sec. 2.1.8 the concept of Renner Teller splitting of degenerate states into one linear and one bent state was introduced. Here it will be shown how the momentum imaging spectrometer can be used to separate these states based on geometry considerations. The two Renner-Teller split states populated after core-excitation of linear molecules have different geometries. As a consequence, ejected fragments will have different distributions with respect to $\vec{\epsilon}$ [90, 91, 25, 92]. Fig. 2.6 presents an example for OCS core-excited to the C $1s^{-1}\pi^*$ state. The main point is the following: The upper branch of the Renner-Teller split state has a linear geometry and the bending motion is constrained within the plane perpendicular to $\vec{\epsilon}$ of the incident light. The lower branch on the other hand has a stable bent geometry and the bending motion is constrained within a plane parallel to the polarization vector. By detecting photo fragments in coincidence after dissociation it is thus possible to probe the geometry of these two states separately by filtering on geometric constraints and measure the bond angle. A filtering was applied on the dissociation channel $O^+/C^+/S^+$ after core-excitation to the C $1s^{-1}\pi^*$ state. To resolve the bent component a routine was written in ANACONDA that selects only coincident events where the center fragment C^+ has a momentum vector within a solid angle $\pm 40°$ about $\vec{\epsilon}$. For the linear component the cross-product for the terminal fragments (O^+ and S^+) momentum vectors within the same solid angle was used. Intensity normalized histograms of the distribution of the angle between terminal fragments for the two RennerTeller split components are compared in Fig. 4.12. The diagram shows that the angles are similar for both states, but the bent component has a smaller average angle, thus confirming the Renner-Teller splitting.

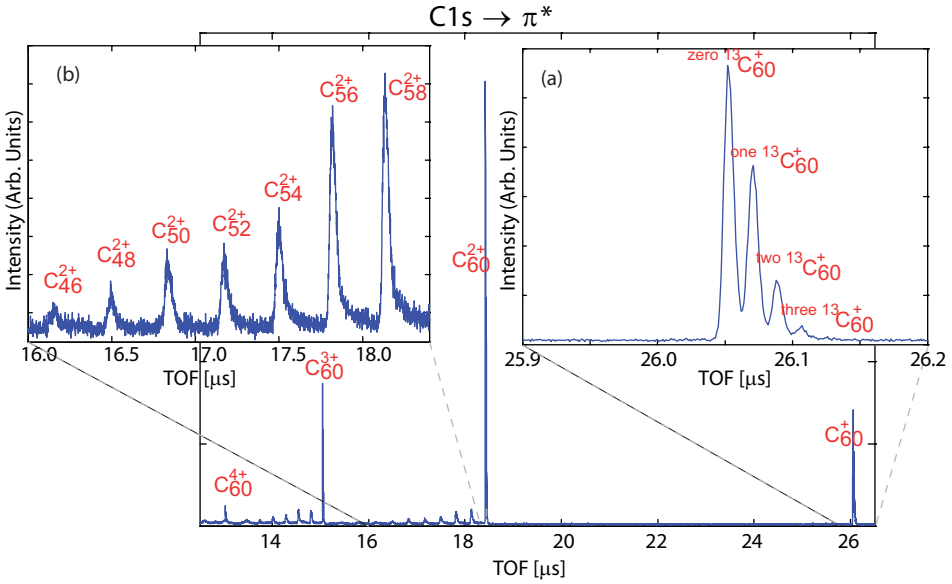

Figure 4.13: TOF spectrum of C_{60}^{q+} fragments after core-excitation to the C $1s^-1\pi^*$ state at 286.2 eV. (a) is expanded view of of fullrene isotopes. (b) Doubly charged fragmented fullerene.

4.3 C_{60}-fullerenes

A consequence of Eq. 3.5 is that as $\frac{m}{q}$ increases, the temporal resolution decreases. This is the main difficulty with TOF mass spectrometry on large molecules. A measure on the mass resolving capability of the spectrometer is therefore how large masses that can be distinguished without

significant overlap. As a demonstration, we look at the relatively large C_{60} fullerene whose lightest isotope has the mass $m = 12 \cdot 60 = 720$ a.u. Fig. 4.13 shows a TOF spectrum after core-excitation to the C $1s^{-1}\pi^*$ state at 286.2 eV. Energy calibration was made by comparing total ion yield with that in Ref. [33]. Up to tetracationic fullerenes are detected. To the left of each undissociated C_{60}^{q+} peak with $q \in \{1 - -4\}$, a progression of even-atomic fragments are visible. This feature is a well-known characteristic since geometry considerations impose a constraint for only even-atomic fullerenes to be stable. Fig. 4.13(a) gives an expanded view of the cation. The peak splitting is due to the isotope distribution. Our design that utilizes a long drift tube as a dispersive element and the high sampling rate of the TDC clearly allows us to distinguish the isotopic shift for the undissociated cation which must have only thermal velocity. The spectrum thus demonstrates the instruments capability to resolve large masses. The TOF peak for C_{60}^{q+} can be seen as a convolution of a line-broadening mechanism, F_{therm}^{q+} due to thermal energy and experimental limitations, and a discrete binomial function, $Bin(60; 0.011)$ where 60 is the number of atoms and 0.011 is the natural abundance of ^{13}C

$$TOF(C_{60}^{q+}) = Bin(60; 0.011) * F_{therm}^{q+} \tag{4.20}$$

F_{exp} can thus be extracted from a fitting procedure as a Gaussian function. From Eq. 4.1 we find the thermal energy to be 3.5 ± 1.5 meV. This is significantly less than the broadening in room temperature of ~ 20 meV, indicating that the cooling is efficient. The measured mass resolution for C_{60} is in agreement with the simulation in Fig. 3.3.

Fragmented species however fails to be resolved due to the KER during breakup. Fragmentation of C_{60} molecules has previously been investigated after electron impact by Foltin *et al* [34] and valence ionization by Katayanagi *et al* [35]. Fig. 4.13(b) shows the primary dissociation channels of the dication C_{60-2n}^{2+} for $n \in \{1 - 7\}$.

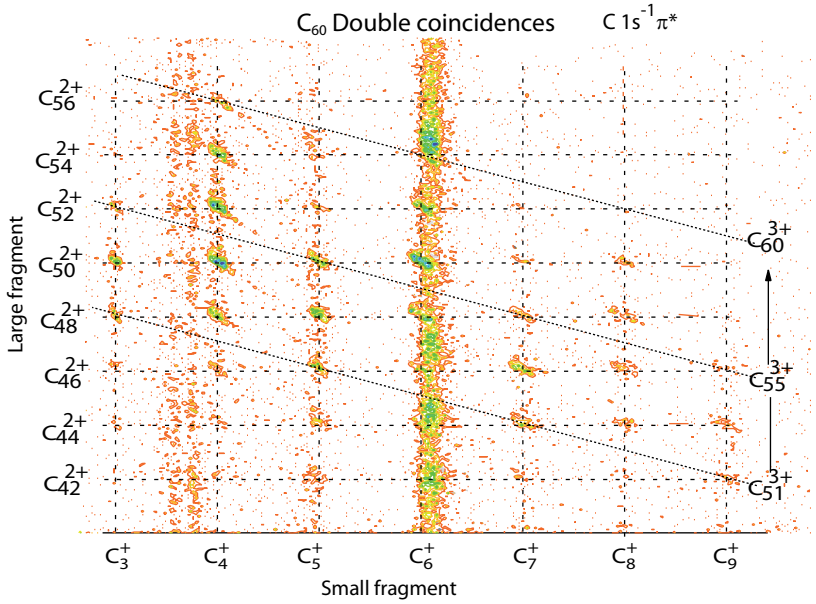

Figure 4.14: PEPIPICO spectrum of fragments from C_{60}^{3+} after core-excitation to the C $1s^{-}1\pi^*$ state at 286.2 eV.

Analysis of fragmentation processes based on only single coincidences can be ambiguous due to the contribution of many unknown fragments. Also double coincidences were registered, see Fig. 4.14. The small fragments C_m for $m \in \{3, 4, 5, ...9\}$ were detected in coincidence with large the fragments C_{60-2n}^{2+} for $n \in \{2, 3, 4...9\}$. The slopes have negative correlation, meaning that they

are true double coincidences. The sum of the ion pair is given as diagonal lines. In cases where the parent ion is not C_{60}^{3+}, also a neutral fragment has been released. It is interesting to observe that parent ions with an odd number of carbon units are detected, considering that they can not be stable [33, 34] The analysis methods described previously in this chapter can be useful to deduce the fragmentation dynamics, which will be done in a coming paper.

Chapter 5

Summary of Papers

5.1 Paper I

The study focuses on the rapid geometry change in ethyne, excited near the carbon 1s edge. Core excitation and ionization leads to population of dicationic states in ethyne. We study three competing dissociation pathways associated with deprotonation in the linear ethyne molecule, and two cases of rapid proton migration. We investigate the alignment of the molecule in the excited state, and find startling differences in these three cases. We present evidence for a strong anisotropy in the production of H_2^+/C_2^+ fragments through a rapid deformation of the molecule to a dibridged conformation with the transition dipole moment parallel to the polarization of the exciting radiation.

5.2 Paper II

The study focuses on the rapid geometry change in core-excited carbonyl sulfide. Excitation to the $C1s^{-1}\pi^*$ and $S2p^{-1}\pi^*$ states is found to induce nuclear mobility that can lead to rearrangement of the molecule. For ejected fragments from two and three body breakups, the anisotropy parameter has been extracted showing that dipole alignment with the polarization vector is preserved, thus dissociation is prompt.

5.3 Paper III

The fragmentation of multiply-charged carbon dioxide is studied after photoexcitation of carbon 1s and oxygen 1s electrons to valence states of π symmetry using a multi-coincidence ion imaging technique. The bent component of the Renner-Teller split states populated in the $1s\rightarrow \pi^*$ resonant excitation opens decay pathways to potential surfaces in highly bent geometries in the dication. Evidence for a complete deformation of the molecule is found in the coincident detection of C^+ and O_2^+ ions. The distinct alignment parallel to the polarization vector indicates rapid deformation and subsequent fragmentation. Investigation of the complete atomization dynamics in the dication leading to asymmetric charge separation shows that the primary dissociation mechanisms, sequential, concerted and asynchronous concerted, are correlated to specific kinetic energies. The study

shows that the bond angle in fragmentation extends below 20°.

5.4 Paper IV

We have studied the dissociation process of the water dication after core-excitation using multi coincidence ion imaging spectroscopy. On resonance we found transient isomerization followed by the two-body breakup H_2^+/O^+. The kinetic energy released to the fragments suggests that the process is initiated from specific dication states and the well-defined angular distribution of the fragments indicates a rapid isomerization process. The angular correlation plots of the three-body breakup $H^+/O^+/H$ provides evidence for the closing of the molecular bond angle at these resonances.

5.5 Paper V

We describe the design and performance of a charged-particle momentum imaging spectrometer optimized for experiments using synchrotron radiation. The spectrometer includes an electrostatic lens for focusing of particles, a long flight tube, large position-sensitive detector and the time-of-flight of particles can be measured using a separate detector which is triggered by Auger electrons or photoelectrons. The focusing of the spectrometer and the equations for optimization of the lens potentials for momentum resolution are described. We discuss the overall performance of the spectrometer for molecules.

5.6 Paper VI

The photo-fragmentation of ammonia clusters ionized with soft x-rays is studied for photon energies above the N-1s edge. The fragments are analyzed with a 3D momentum mass spectrometer to access the energy and angular correlations between fragments. By choosing the cluster sizes below or above the critical size of stable dication, we can interpret our observation as result of the fission of the cluster and the charge migration due the ultra-fast proton mobility.

Bibliography

[1] J. M. Hollas, *Modern Spectroscopy, Fourth Edition, pp. 27–34*, Wiley, 2000.

[2] N. Saito, F. Heiser, O. Hemmers, K. Wieliczek, J. Viefhaus, and U. Becker, *Phys. Rev. A* **54**, 2004 (1996).

[3] I. Hjelte, M. N. Piancastelli, R. Fink, O. Björneholm, M. Bässler, R. Feifel, A. Giertz, H. Wang, K. Wiesner, and A. Ausmees, *Chem. Phys. Lett.* **334**, 151 (2001).

[4] T. A. Carlson and M. O. Krause, *Phys. Rev. Lett.* **14**, 390 (1965).

[5] J. Palaudoux, P. Lablanquie, L. Andric, J. H. D. Eland, and F. Penent, in *J. Phys.: Conference Series*, volume 141, p. 012012, 2008.

[6] D. Winkoun, G. Dujardin, L. Hellner, and M. Besnard, *J. Phys. B: At. Mol. Opt. Phys.* **21**, 1385 (1988).

[7] J. H. D. Eland, *Chem. Phys.* **323**, 391 (2006).

[8] J. H. D. Eland, *Chem. Phys.* **290**, 27 (2003).

[9] J. Laskin and C. Lifshitz, *J. Mass Spectrom.* **36**, 459 (2001).

[10] L. Journel, R. Guillemin, A. Haouas, P. Lablanquie, F. Penent, J. Palaudoux, L. Andric, M. Simon, D. Céolin, T. Kaneyasu, J. Viefhaus, M. Braune, W. B. Li, C. Elkharrat, F. Catoire, J.-C. Houver, and D. Dowek, *Phys. Rev. A* **77**, 1 (2008).

[11] W. L. Borst and E. C. Zipf, *Phys. Rev. A* **3**, 979 (1971).

[12] A. E. Slattery, T. a. Field, M. Ahmad, R. I. Hall, J. Lambourne, F. Penent, P. Lablanquie, and J. H. D. Eland, *J. Chem. Phys.* **122**, 84317 (2005).

[13] N. Saito, A. De Fanis, I. Koyano, and K. Ueda, *Physica Scripta* **110**, 90 (2004).

[14] J. Adachi, N. Kosugi, E. Shigemasa, and A. Yagishita, *J. Chem. Phys.* **107**, 4919 (1997).

[15] J. N. Israelachvili, *Intermolecular and surface forces*, Academic press, 2000.

[16] R. N. Zare and D. R. Herschbach, *Proc. IEEE* **51**, 173 (1964).

[17] D. R. Herschbach, *Adv. Chem. Phys.* **10**, 319 (1966).

[18] R. N. Zare, *Mol. Photochem.* **4**, 1 (1972).

[19] A. I. Chichinin, T. S. Einfeld, K. H. Gericke, and C. Maul, *Imaging in Molecular Dynamics*, Cambridge University Press, 2003.

[20] J. Laksman, D. Céolin, M. Gisselbrecht, S. E. Canton, and S. L. Sorensen, *J. Chem. Phys.* **131**, 244305 (2009).

[21] J. Laksman, D. Céolin, M. Gisselbrecht, and S. L. Sorensen, *J. Chem. Phys.* **133**, 144314 (2010).

[22] J. Stöhr, *NEXAFS Spectroscopy*, Springer Verlag, 1992.

[23] J. Solomon, C. Jonah, P. Chandra, and R. Bersohn, *J. Chem. Phys.* **55**, 1908 (1971).

[24] R. Renner, *Z. Phys. **92**, 172 (1934) (in German). English translation in H. Hettema, Quantum Chemistry, Classic Scientific Papers, World Scientific* **92**, 172 (1934).

[25] Y. Muramatsu, K. Ueda, N. Saito, H. Chiba, M. Lavollee, A. Czasch, T. Weber, O. Jagutzki, H. Schmidt-Böcking, R. Moshammer, U. Becker, K. Kubozuka, and I. Koyano, *Phys. Rev. Lett.* **88**, 2 (2002).

[26] K. C. Prince, L. Avaldi, M. Coreno, R. Camilloni, and M. Simone, *J. Phys. B: At. Mol. Opt. Phys.* **32**, 2551 (1999).

[27] B. H. Bransden and C. J. Joachain, *Physics of Atoms and Molecules*, Prentice Hall, 2000.

[28] V. Brems, B. M. Nestmann, and S. D. Peyerimhoff, *Chem. Phys. Lett.* **287**, 255 (1998).

[29] R. Thissen, J. Delwiche, J. M. Robbe, D. Duflot, J. Flament, and J. H. D. Eland, *J. Chem. Phys.* **99**, 6590 (1993).

[30] R. L. Johnston, *Atomic and Molecular Clusters*, Taylor & Francis, 2002.

[31] H. Nakai, T. Goto, T. Ichikawa, Y. Okada, T. Orii, and K. Takeuchi, *Chem. Phys.* **262**, 201 (2000).

[32] M. Gisselbrecht, J. Laksman, E. Månsson, C. Grunewald, A. Sankari, M. Tchaplyguine, O. Björneholm, , and S. L. Sorensen, Fission in liquid ammonia: from nano-droplet to a few molecules, 2012.

[33] S. Aksela, E. Nommiste, J. Jauhiainen, E. Kukk, J. Karvonen, H. Berry, S. L. Sorensen, and H. Aksela, *Phys. Rev. Lett.* **75**, 2112 (1995).

[34] M. Foltin, O. Echt, P. Scheier, B. Dunser, R. Worgotter, D. Muigg, S. Matt, and T. D. Mark, *J. Chem. Phys.* **107**, 6246 (1997).

[35] H. Katayanagi and K. Mitsuke, *J. Chem. Phys.* **133**, 081101 (2010).

[36] A. Lindgren, *Studies of Molecular and Cluster Fragmentation Using Synchrotron Radiation: Measurements and Models*, PhD thesis, Lund University, 2006.

[37] W. Wiley and I. McLaren, *Rev. Sci. Instrum.* **26**, 1150 (1955).

[38] J. H. D. Eland, *Int. J. Mass Spec. Ion Proc.* **8**, 143 (1972).

[39] J. H. D. Eland, *Int. J. Mass Spec. Ion Proc.* **12**, 389 (1973).

[40] J. H. D. Eland, *Rev. Sci. Instrum.* **49**, 1688 (1978).

[41] J. H. D. Eland, *J. Chem. Phys.* **70**, 2926 (1979).

[42] J. H. D. Eland, F. S. Wort, and R. N. Royds, *J. Electr. Spectr. Rel. Phenom.* **41**, 297 (1986).

[43] J. H. D. Eland, *Mol. Phys.* **61**, 725 (1987).

[44] J. H. D. Eland, *Acc. Chem. Res.* **22**, 381 (1989).

[45] J. H. D. Eland, *Laser Chem.* **11**, 259 (1991).

[46] J. H. D. Eland, *Meas. Sci. Technol.* **4**, 1522 (1993).

[47] J. H. D. Eland, *Meas. Sci. Technol.* **5**, 1501 (1994).

[48] S. Hsieh and J. H. D. Eland, *J. Phys. B: At. Mol. Opt. Phys.* **29**, 5795 (1996).

[49] K. Ueda, E. Shigemasa, Y. Saito, A. Yagashita, T. Sasaki, and T. Hayaishi, *Rev. Sci. Instrum.* **60**, 2193 (1989).

[50] D. Chandler and P. Houston, *J. Chem. Phys.* **87**, 1445 (1987).

[51] A. T. J. B. Eppink and D. H. Parker, *Rev. Sci. Instrum.* **68**, 3477 (1997).

[52] J. H. D. Eland and A. Pearson, *Meas. Sci. Technol.* **1**, 36 (1990).

[53] *Roentdek: MCP Delay Line Detector Manual*, 2007.

[54] K. Ueda and J. H. D. Eland, *J. Phys. B: At. Mol. Opt. Phys.* **38**, S839 (2005).

[55] D. Céolin, C. Miron, M. Simon, and P. Morin, *J. Elec. Spect. Rel. Phen.* **141**, 171 (2004).

[56] D. Céolin, G. Chaplier, M. Lemonnier, G. a. Garcia, C. Miron, L. Nahon, M. Simon, N. Leclercq, and P. Morin, *Rev. Sci. Instrum.* **76**, 043302 (2005).

[57] *Autodesk Inventor, Web-Site: www.autodesk.se*, 2001.

[58] G. Prümper, X. J. Liu, H. Fukuzawa, K. Ueda, V. Carravetta, J. Harries, Y. Tamenori, and S. Nagaoka, *J. Phys.: Conference Series* **88**, 012008 (2007).

[59] D. A. Dahl, *Simion 3D version 7.0 User's manual*, 2000.

[60] *CAEN MOD. N 470, 4 CHANNEL PROGRAMMABLE H.V. POWER SUPPLY, Web-Site: www.caen.it*, 2002.

[61] D. P. Seccombe and T. J. Reddish, *Rev. Sci. Instrum.* **72**, 1330 (2001).

[62] M. Bässler, A. Ausmees, M. Jurvansuu, R. Feifel, J.-O. Forsell, P. de TarsoFonseca, A. Kivimäki, S. Sundin, S. L. Sorensen, R. Nyholm, O. Björneholm, S. Aksela, and S. Svensson, *Nucl. Instrum. and Meth.* **469**, 382 (2001).

[63] S. Aksela, a. Kivimaki, O.-P. Sairanen, a. Naves de Brito, E. Nommiste, and S. Svensson, *Rev. Sci. Instrum.* **66**, 1621 (1995).

[64] L. Frasinski, M. Stankiewicz, P. Hatherly, and K. Codling, *Meas. Sci. Technol.* **3**, 1188 (1992).

[65] *Open, high vacuum imaging. MCP Detector Systems, Web-Site: www.proxitronic.de*, 2009.

[66] U. Zimmermann, N. Malinowski, U. Näher, S. Frank, and T. P. Martin, *Z. Phys. D* **31**, 85 (1994).

[67] C. Ellert, M. Schmidt, C. Schmitt, and T. Reiners, *Phys. Rev. Lett.* **75**, 1731 (1995).

[68] K. Hansen, H. Hohmann, R. Muller, and E. E. B. Campbell, *The Journal of Chemical Physics* **105**, 6088 (1996).

[69] Thermocoax, *Heating Element: Single core with cold ends: ZEZ and ZUZ types, Web-site: www.thermocoax.com*, 2012.

[70] V. Brites, J. H. D. Eland, and M. Hochlaf, *Chem. Phys.* **346**, 23 (2008).

[71] M. Simon, M. Lavollee, M. Meyer, and P. Morin, *J. Elec. Spect. Rel. Phen.* **79**, 401 (1996).

[72] M. Simon, T. Lebrun, R. Martins, G. G. B. de Souza, I. Nenner, M. Lavollee, and P. Morin, *J. Phys. Chem.* **97**, 5228 (1993).

[73] P. Erman, A. Karawajczyk, E. Rachlew, M. Stankiewicz, and K. Franzén, *J. Chem. Phys.* **107**, 10827 (1997).

[74] J. Adachi, N. Kosugi, E. Shigemasa, and A. Yagishita, *Chem. Phys. Lett.* **309**, 427 (1999).

[75] J. Adachi, K. Hosaka, T. Teramoto, M. Yamazaki, N. Watanabe, M. Takahashi, and A. Yagishita, *J. Phys. B: At. Mol. Opt. Phys.* **40**, F285 (2007).

[76] R. E. Continetti, *Annu. Rev. Phys. Chem.* **52**, 165 (2001).

[77] J. D. Savee, J. E. Mann, and R. E. Continetti, *J. Phys. Chem. A* **113**, 3988 (2009).

[78] A. A. Hoops, J. R. Gascooke, A. E. Faulhaber, K. E. Kautzman, and D. M. Neumark, *J. Phys. Chem.* **120**, 7901 (2004).

[79] C. M. Laperle, J. Mann, T. G. Clements, and R. Continetti, *Phys. Rev. Lett.* **93**, 153202 (2004).

[80] M. Lebech, J. C. Houver, and D. Dowek, *Rev. Sci. Instrum.* **73**, 1866 (2002).

[81] A. Matsuda, E. Takahashi, and A. Hishikawa, *J. Chem. Phys.* **127**, 114318 (2007).

[82] R. H. Dalitz, *Philos. Mag.* **44**, 1068 (1953).

[83] C. Maul and K. H. Gericke, *J. Phys. Chem. A* **104**, 2531 (2000).

[84] D. Babikov, E. A. Gislason, M. Sizun, F. Aguillon, V. Sidis, M. Barat, J. C. Brenot, J. A. Fayeton, and Y. J. Picard, *J. Chem. Phys.* **116**, 4871 (2002).

[85] T. G. Clements, A. K. Luong, H.-J. Deyerl, and R. E. Continetti, *J. Chem. Phys.* **114**, 8436 (2001).

[86] A. De Fanis, M. Oura, N. Saito, M. Machida, M. Nagoshi, A. Knapp, J. Nickles, A. Czasch, R. Dörner, Y. Tamenori, H. Chiba, M. Takahashi, J. H. D. Eland, and K. Ueda, *J. Phys. B: At. Mol. Opt. Phys.* **37**, L235 (2004).

[87] S. D. Price, *Int. J. Mass Spec.* **260**, 1 (2007).

[88] Z. D. Pešič, D. Rolles, R. C. Bilodeau, I. Dimitriu, and N. Berrah, *Phys. Rev. A* **78**, 051401 (2008).

[89] T. Masuoka, *Phys. Rev. A* **50**, 3886 (1994).

[90] E. Kukk, *AIP Conference Proceedings* , 163 (2000).

[91] Y. Muramatsu, *Chem. Phys. Lett.* **330**, 91 (2000).

[92] Y. Muramatsu, K. Ueda, and H. Chiba, *Surf. Rev. Lett.* (2002).